

May 28, 1999

RESEARCH AND DEVELOPMENT REPORT

PEBB Thermal Management Interim Report

Prepared by

Dr. Peter N. Harrison and Richard W. Garman

A&T Engineering Technologies, VECTOR Research Division

Distribution authorized to U.S. Government agencies and their
contractors only; Test and Evaluation use; May 1999. Other requests for
this document shall be referred to the Carderock Division of the Naval
Surface Warfare Center (Code 813).

May 28, 1999

RESEARCH AND DEVELOPMENT REPORT

PEBB Thermal Management Interim Report

Prepared by
Dr. Peter N. Harrison and Richard W. Garman
A&T Engineering Technologies, VECTOR Research Division
307 Greenlee Road
Annapolis, Maryland 21402-5067

Prepared for
Carderock Division Naval Surface Warfare Center
Electrical and Cable Technology Branch (Code 813)
Annapolis, Maryland 21402-5067

Contract N00167-96-D-0045
Delivery Order No. 0088

ABSTRACT

A critical factor affecting the operating life and limitations of a power semiconductor is the temperature of its junction. Numerous heat sinks and heat transfer devices have been designed and developed to remove heat from power semiconductors. The present forced convection water based designs used in the Power Electronic Building Blocks (PEBB) program do not allow the full power potential of the switching devices to be utilized. To support the PEBB program, VECTOR Research Division developed a plan to experimentally and analytically characterize the thermal performance of water-cooled heat sink technologies. The primary measures of the performance of the heat sinks are the thermal impedance and the systems level parameters of flow rate and pressure drop. A simple open chambered water-cooled heat sink will serve as the baseline for this comparison. This heat sink is similar to the housing for the PEBB 1.5 without the copper sponge. Other designs identified for characterization are the Harris Corporation PEBB 1 baffled cavity and the PEBB 1.5 copper sponge heat sinks and the Coriolis Corporation curved surface cooling design. This document provides a synopsis of the test platform and approach. Test results of the open chambered water-cooled heat sink, the Harris PEBB 1 baffled cavity heat sink, the same heat sink with minor modifications, and a simple four pass channel design are covered under this report.

TABLE OF CONTENTS

Abstract	iii
List Of Figures.....	vi
List Of Equations.....	viii
Administrative Information	viii
Summary	1
Introduction	3
BACKGROUND.....	3
TEST OBJECTIVES	4
Approach	5
CHARACTERIZING THERMAL PERFORMANCE	5
TEST APPARATUS.....	7
CALIBRATION	11
<i>Resistor Emissivity</i>	11
<i>Resistor Uniformity</i>	12
<i>Radiated and Convected Heat Flux</i>	16
<i>Fixture Pressure Drop</i>	17
TEST PROCEDURE	18
<i>Thermal Impedance</i>	18
<i>External Systems Requirements</i>	19
DATA REDUCTION.....	20
Preliminary Results	24
BASELINE HEAT SINK	24
<i>Thermal Impedance</i>	25
<i>External System Requirements</i>	29
HARRIS PEBB 1 BAFFLED.....	30
<i>Thermal Impedance</i>	31
<i>External System Requirements</i>	34
MODIFIED HARRIS PEBB 1 BAFFLED	35
<i>Thermal Impedance</i>	36

<i>External System Requirements</i>	39
CHANNELED	39
<i>Thermal Impedance</i>	40
<i>External System Requirements</i>	44
HEAT SINK COMPARISON	44
Conclusions and Future Work	50
References	53
Appendix A. Unit Conversions.....	54
Notation.....	55

LIST OF FIGURES

Figure 1. Schematic of generic heat sink.	6
Figure 2. Thermal management test fixture.	6
Figure 3. Thermal management laboratory schematic.	7
Figure 4. Schematic of thick film resistor.....	8
Figure 5. Thick film resistor assembly.....	9
Figure 6. PEBB 1 assembly with PEBB 1 housing.....	9
Figure 7. Resistor Emissivity Calibration Test.	12
Figure 8. Schematic of resistor uniformity test apparatus.....	13
Figure 9. Sample thermal images showing varying results from uniformity pulse testing (spot in center is reflection of camera lens)	14
Figure 10. Sample thermal image from uniformity pulse testing with camera rotated 90° (spot in center is reflection of camera lens).	14
Figure 11. Uniformity pulse testing image.....	15
Figure 12. Image of unheated TFR showing infrared reflections.	16
Figure 13. Graph showing uniformity pulse test results.....	16
Figure 14. Radiated and convected heat loss from the top of the TFR vs. surface temperature. .	18
Figure 15. Thermal conductivity vs. temperature for 96% alumina.	23
Figure 16. Baseline heat sink.....	24
Figure 17. Two open chambered heat sink temperature distributions at 0.5 gpm flow rate and 400 W dissipation taken moments apart.	25

Figure 18. Open chambered heat sink temperature distribution at 3.4 gpm flow rate and 800 W dissipation.....	26
Figure 19. Open chambered heat sink average thermal impedance vs. heat flux density.	27
Figure 20. Open chambered heat sink average thermal impedance vs. coolant flow rate.....	28
Figure 21. Open chambered heat sink thermal impedance standard deviation vs. flow rate.....	29
Figure 22. Pressure drop vs. flow rate for open chambered heat sink.	30
Figure 23. Harris PEBB 1 baffled heat sink.....	31
Figure 24. Harris PEBB 1 heat sink temperature distribution at 3.0 gpm flow rate and 1.0 kW dissipation.....	32
Figure 25. Harris PEBB 1 heat sink average thermal impedance vs. heat flux density.	33
Figure 26. Harris PEBB 1 heat sink average thermal impedance vs. coolant flow rate.....	33
Figure 27. Harris PEBB 1 heat sink thermal impedance standard deviation vs. flow rate.....	34
Figure 28. Pressure drop vs. flow rate for Harris PEBB 1 heat sink.	35
Figure 29. Modified Harris PEBB 1 baffled heat sink.	36
Figure 30. Modified Harris PEBB 1 heat sink temperature distribution at 2.9 gpm flow rate and 800 W dissipation.	36
Figure 31. Modified Harris PEBB 1 heat sink average thermal impedance vs. heat flux density.....	37
Figure 32. Modified Harris PEBB 1 heat sink average thermal impedance vs. coolant flow rate.....	38
Figure 33. Modified Harris PEBB 1 heat sink thermal impedance standard deviation vs. flow rate.....	38
Figure 34. Pressure drop vs. flow rate for modified Harris PEBB 1 heat sink.	39
Figure 35. Channeled heat sink.....	40
Figure 36. Channeled heat sink temperature distribution at 2.0 gpm flow rate and 600 W dissipation.....	41
Figure 37. Channeled heat sink average thermal impedance vs. heat flux density.	42
Figure 38. Channeled heat sink average thermal impedance vs. coolant flow rate.....	43
Figure 39. Channeled heat sink thermal impedance standard deviation vs. flow rate.	43
Figure 40. Pressure drop vs. flow rate for channeled heat sink.	44
Figure 41. Average thermal impedance vs. flow rate comparison.	45
Figure 42. Thermal impedance standard deviation vs. flow rate comparison.....	46
Figure 43. Average thermal impedance plus one standard deviation vs. flow rate comparison. .	47
Figure 44. Pressure drop vs. flow rate comparison.	48
Figure 45. Comparison of average thermal impedance plus one standard deviation vs. pumping power.....	49
Figure 46. Comparison of average thermal impedance plus one standard deviation vs. pumping power (log scale).....	49

LIST OF EQUATIONS

(1) Thermal impedance.	5
(2) Biot number	10
(3) Heat flux due to radiated and convected losses	17
(4) Heat flux of the heat sink interface	20
(5) Heat flux generated by the thick film resistor	20
(6) Thermal impedance of the heat sink	21
(7) Heat sink thermal impedance (summarized)	21
(8) Total thermal impedance	21
(9) Thermal impedance of the TFR/substrate combination.....	21
(10) Heat flux of the heat sink interface	22
(11) Average temperature of the alumina substrate	22
(12) Average temperature of the alumina substrate (simplified).....	22
(13) Fourier's Law of heat conduction	22
(14) Estimated average temperature of alumina substrate	22
(15) Estimated thermal impedance of the TFR/substrate combination	23

ADMINISTRATIVE INFORMATION

This work was performed under contract number N00167-96-D-0045 (delivery order number 0088) as part of the Power Electronic Building Blocks (PEBB) program. The work was sponsored by the Carderock Division of the Naval Surface Warfare Center (NSWCCD), Code 813, Mr. Stephen Smith. All work contained in this test plan was performed by A&T Engineering Technologies, VECTOR Research Division, Machinery Systems Department.

SUMMARY

The purpose of this investigation is to provide experimental and analytical results to the PEBB program for use in evaluating existing and proposed thermal management solutions for both active and passive components of the power converters being developed. This preliminary report presents some of the experimental results from the investigation and covers water-cooling of PEBB power semiconductor modules.

Four different heat sinks have been tested thus far, an open or hollow chambered configuration, the original Harris PEBB 1 heat sink, a modified version of the Harris PEBB 1, and a simple four pass channelled heat sink. The open chambered heat sink was included as a baseline that can be modeled with simple analytical expressions. It also serves as a point of comparison for the performance of the other designs. The original Harris PEBB 1 heat sink was the first water cooled heat sink used in the PEBB program and was suspected of being a weak link in the thermal management of that generation of power converter. It was designed to attach to the bottom of a PEBB power module and channel cooling water flow in contact with the bottom of the module through a labyrinth type path. Simple modifications were made to the original PEBB 1 design to reduce the amount of coolant flow that was allowed to bypass a large part of the channel by flowing between the tops of the baffles and the module baseplate. The last heat sink tested was another design utilizing baffles to channel the water flow through a labyrinth type path; however, the channel layout on this design was simpler than the PEBB 1 designs and improvements were made to reduce the back pressure.

Testing of the heat sinks was performed using VECTOR Research Division's thermal management test stand. Temperature and flow rate controlled cooling water was passed through the heat sinks while attached to a resistive thermal load. The resistor used was a large (16.7 cm²) thick film resistor (TFR) approximately the size of the die attachment area of a PEBB power module baseplate printed on an alumina substrate slightly larger than the PEBB baseplate. In the four heat sinks tested thus far, the cooling water was in direct contact with the alumina, just as it would be in contact with an actual PEBB module baseplate. The TFR acted as a uniformly distributed heat source and therefore measurement of the temperature distribution across the top of it allowed the determination of the cooling distribution provided by the heat sink. This temperature distribution was measured using an infrared (IR) thermal imaging cameraⁱ.

ⁱ The IR thermal imaging camera is the property of the Naval Surface Warfare Center, Carderock Division, Code 813.

The measure of the performance of the heat sinks used in this study was the thermal impedance, θ . Equal to the reciprocal of the film or convection heat transfer coefficient (h) the thermal impedance can vary over the heat sink interface with the heat source. This is the characteristic that distinguishes it from the thermal resistance, a lumped parameter typically given by heat sink and power module manufacturers. The fact that it can vary over the interface makes the thermal impedance more useful in assessing the effectiveness of a heat sink by allowing the cooling uniformity to be quantified. The thermal impedance distribution can also be utilized in determining the best locations for the silicon dies.

Four different calibrations were done prior to testing the heat sinks. The emissivity of the TFR was measured over the temperature range to be encountered during testing to allow the infrared thermal imaging camera to accurately measure the temperature distribution. The uniformity of the resistivity of the TFR was assessed in order to determine if it was a uniform heat source. The amount of energy leaving the resistor from the top via radiation and convection rather than through the heat sink was determined as a function of the resistor temperature. Finally, the test fixture pressure drop was measured versus cooling water flow rate so that it can be accounted for when measuring the heat sink pressure drop.

Testing of each heat sink was conducted over a range of flow rates and resistive heating levels. At each test point, the test conditions were recorded. The temperature distribution over the TFR was recorded using the infrared camera and the pressure drop was measured using dial gages. The thermal data from the infrared camera was in the form of a digital file with a temperature value for each pixel of the thermal image. The data was reduced and plotted using Microsoft Excel.

Results from the testing revealed that the open chambered configuration used was not as good a baseline as expected. The suspected uniformity deficiencies of the original PEBB 1 heat sink were made readily apparent with the thermal images and were quantified by the standard deviation of the thermal impedance distribution. The modifications made to the PEBB 1 heat sink produced significant improvements in its performance; however, a small region remained ineffectively cooled. The simple channeled heat sink performed poorly at low flow rates, but improved to the point that it was at or near the best of the four at higher flow rates.

The results of the tests conducted for this project proved to be very useful in assessing the performance of the heat sinks and in determining ways to improve the designs. By seeing the distribution of the cooling provided by the different heat sinks at different flow rates, problem areas were easily identified and possible solutions were more apparent. While a few changes could be made to improve the results obtained, the basic methodology appears to be quite sound.

INTRODUCTION

A critical factor affecting the operating life and limitations of a power semiconductor is the temperature of its junction. Numerous heat sinks and heat transfer devices have been designed and developed to remove heat from power semiconductors. This document provides preliminary results from an effort to experimentally characterize the thermal performance of water-cooled heat sink technologies applicable to the PEBB program. The primary measures of the performance of the heat sinks are the thermal impedance and the systems level parameters of flow rate required and associated pressure drop. The results from this experimental test program will be correlated with a parallel analytical effort. A simple open chambered water-cooled heat sink serves as the baseline for this comparison. Other designs identified for characterization are the Harris Corporationⁱⁱ PEBB 1 baffled cavity and PEBB 1.5 copper sponge heat sink and the Coriolis Corporationⁱⁱⁱ curved surface cooling design. This document provides a summary description of the test platform, the calibration and test procedures, and test results for the aforementioned devices, except for the copper sponge and curved surface designs.

Background

Heat generated in power semiconductor devices due to current flow and voltage drop must be removed to control the junction temperature. Through effective removal of heat from the junction, the power handling of the device can be maximized. Conversely, if adequate cooling is not provided, the device will fail prematurely. For the PEBB HTP devices (both MCT and IGBT), this heat is conducted through the silicon, a copper conductor, solder and metalization interfaces, and an aluminum nitride baseplate to an attached water-cooled heat sink.

Harris Corporation provided the original heat sink for thermal management in high power applications of PEBB 1. This heat sink bolts to the bottom of the module and allows direct contact of the water with the metalized aluminum nitride baseplate within a baffled cavity. However, this heat sink design was found to perform poorly in terms of both effectiveness and efficiency. The primary deficiency in effectiveness is the existence of hot spots on the baseplate due to areas of relatively stagnant flow. The poor efficiency of the heat sink manifests itself in a large pressure drop across it. In order to create the boundary layer turbulence required to obtain sufficient device cooling, water flow rates over 3 gpm are needed and the resulting pressure drop

ⁱⁱ This division of Harris was purchased by Silicon Power Corporation (SPCO), 252 Welsh Pool Road, Exton, PA 19341

ⁱⁱⁱ Coriolis Corporation, 15315 Sobey Road, Saratoga, CA 95070.

is greater than 25 psi across the heat sink. This relatively large pressure drop must be overcome by a higher power-circulating pump in the closed loop system and results in increased costs.

Harris Corporation's approach to improving the heat sink performance in their development of PEBB 1.5 devices was to replace the baffles with a metallic (copper) sponge-like material attached to the module baseplate with a good thermal bond. Harris' preliminary results with this design show significant improvements in cooling capability, uniformity, and pressure drop. However, this approach may have drawbacks in the areas of longevity and practicality. Because of the relatively delicate structure of the sponge, erosion of the material will likely affect the cooling over an extended period of operation. On the practical side, by requiring the sponge to be attached to the baseplate of the module, assembly costs will likely increase. One of the reasons for this effort is to identify a better solution to the thermal management of the PEBB modules than either the present baffled or metallic sponge heat sinks.^{iv}

Test Objectives

There are three main objectives of the VECTOR Research PEBB thermal management baseline study. These objectives are:

1. To characterize the performance of presently available PEBB water-cooled heat sinks in a consistent manner to provide a quantitative means of comparing various designs.
2. To develop basic analytical models of presently available heat sinks, correlate them with experimental results, and use them in parametric and scaling analyses of the designs.
3. To use the results of the first two objectives to improve thermal management of present and future PEBB devices being used in both low and high power applications. Heat sink designs should be capable of dissipating up to 1400 watts from a module inexpensively with long life and low maintenance.

This interim report will focus on the first objective.

^{iv} "Improved Thermal Management of PEBB Devices and Systems (VECTOR Research Subtask 8b)," VECTOR Research (Dec 1997).

APPROACH

The thermal management experimental testing is being performed in parallel with an analytical effort. These two approaches to evaluating PEBB heat sinks will be correlated as they progress in order to validate the analytical models. In each case, the primary quantities desired to characterize the performance of a particular heat sink are:

- Thermal impedance distribution over the cooling interface of the heat sink,
- Dependence of the thermal impedance on the fluid flow rate and heat transfer rate per unit area (heat flux),
- Pressure drop versus the flow rate of the cooling fluid.

In addition, the issue of how a particular heat sink's performance scales will also be examined. This will be useful for answering questions such as "what is the best approach for cooling a device producing twice the thermal load?" Determination of these quantities will provide designers with the data they need to determine the thermal resistance for their device/heat sink combination and which cooling approach is the most appropriate and cost effective for their PEBB application.

Characterizing Thermal Performance

The thermal impedance is being used as the primary quantification of heat sink performance because it provides a basic measure of how the sink performs, independent of the heat source. It is defined as the temperature differential required for a unit heat flux and has the expression

$$\theta(x, y) = \frac{T(x, y) - T_F}{(q/A)_{\text{sink}}(x, y)}, \quad (1)$$

where $T(x, y)$ is the temperature distribution over the heat sink interface with the heat source, T_F is the inlet temperature of the cooling fluid, and $(q/A)_{\text{sink}}(x, y)$ is the heat transfer rate per unit area through the interface. From this expression, it can be seen that the thermal impedance and heat transfer rate per unit area are spatially varying quantities defined over the interface. In contrast, the thermal resistance is a single value that is determined in a manner that allows the use of an electrical analogy in thermal calculations for a specific device/heat sink combination. The thermal resistance can be approximated by dividing the thermal impedance by the area of the heat source. Figure 1 is a schematic of a heat sink with the thermal impedance equation terms shown. It is worth noting that the thermal impedance (θ) is the reciprocal of the effective film coefficient (h).

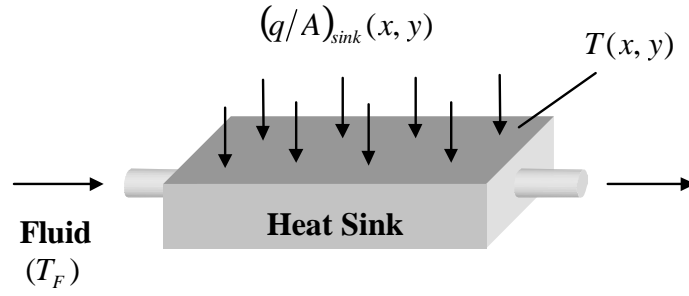


Figure 1. Schematic of generic heat sink.

Experimental determination of the thermal impedance, therefore, involves the measurement of the cooling fluid input temperature, the temperature distribution over the interface between the heat sink and a thermal load, and the heat flux across the same interface under the load. Measurement of the fluid temperature is straightforward and was made using a thermistor probe. The remaining quantities are determined based on measurements made using the test fixture shown in Figure 2. It consists of a thick film resistor (TFR) with uniform sheet resistivity over its area as a heat source, the heat sink under test, and an infrared thermal-imaging camera for temperature measurement. The temperature distribution on the top of the TFR, $T_{TFR}(x, y)$, is measured with the infrared camera. The calculation procedure for determining the thermal impedance of the sink is presented in the data reduction section.

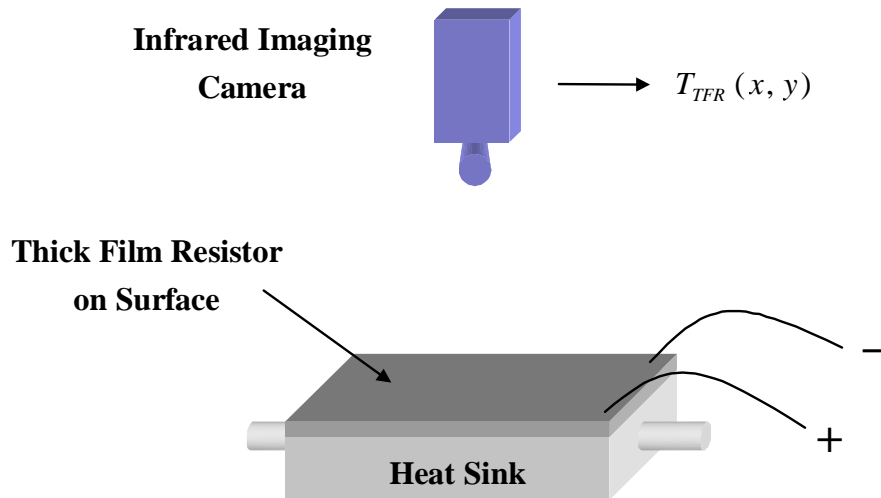


Figure 2. Thermal management test fixture.

Test Apparatus

The thermal management laboratory facility consists of three subsystems. These subsystems are the water feed system, the heat source, and the instrumentation. A schematic of the laboratory set-up is shown in Figure 3.

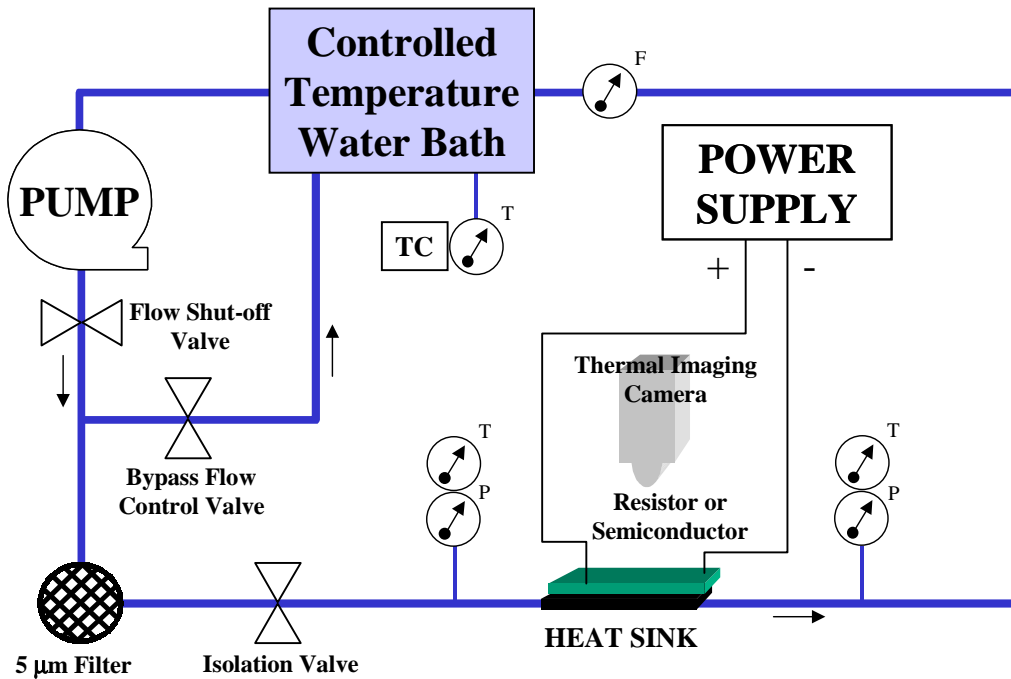


Figure 3. Thermal management laboratory schematic.

The water feed system consists of a cold water bath chiller, temperature controller, pump, flow shut-off valve, flow meter, bypass flow control valve, 0.5 μm water filter, and miscellaneous hoses and piping. The bath chiller and temperature controller provide a supply water reservoir at a constant temperature. The temperature controller is connected to a type-J thermocouple immersed in the chiller bath and cycles the chiller's compressor motor to regulate the reservoir temperature. The pump, flow shut-off valve, and bypass flow control valve provide a controlled water flow to the heat sink.

The heat source is a TFR approximately the size of the cooled area of the PEBB baseplate connected to a power supply. Figure 4 is a schematic of the resistor. The resistor material is printed on an alumina substrate that is slightly larger than the aluminum nitride baseplates used by Harris in the PEBB 1 and PEBB 1.5 modules. The reason for the increased size for the alumina is to provide space for attaching terminals (see Figure 5) to the resistor while still having the resistor approximately the size of the area cooled by PEBB 1 heat sink. Alumina is being used instead of aluminum nitride because the resistor material does not adhere well to aluminum

nitride. Metalized solder pads are located at each end of the resistor to allow the attachment of sheet metal copper terminals, which span the depth of the resistor. The baseplate is also metalized on the non-resistor side, as is the Harris aluminum nitride, to allow soldering of the metallic sponge, curved surface, or similar heat sinks. The resistor assembly was fabricated by Hybrid-Tek, Inc.^v using ESL 3981 cermet resistor material and ESL 9562 cermet platinum palladium silver metalization printed and fired onto a 60 mil thick Coors ADS-96R alumina 96% substrate. The resistance of the TFR is nominally 12.5 Ω and the manufacturer specifies a coefficient of variation of less than 4%.

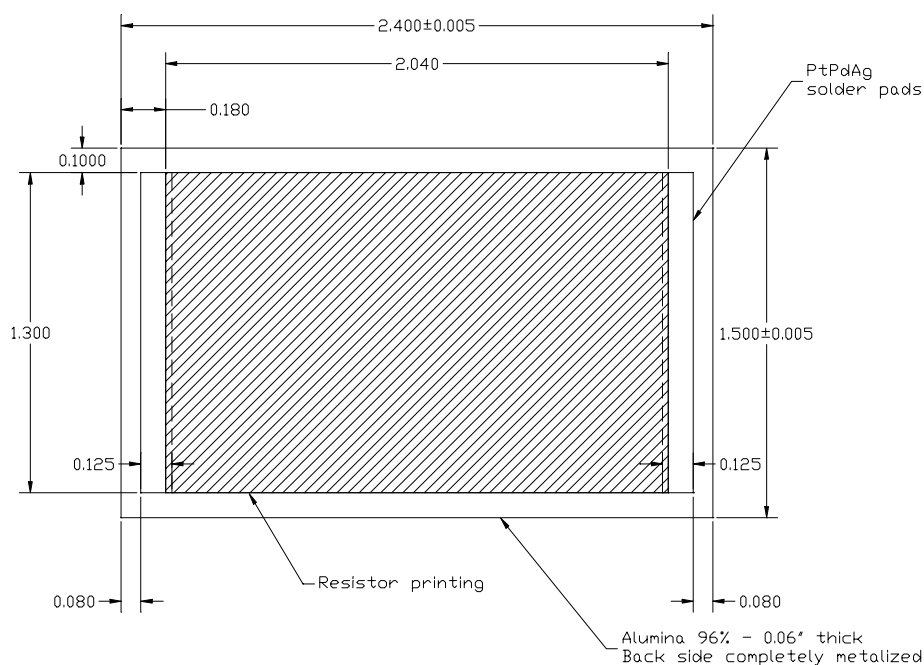


Figure 4. Schematic of thick film resistor.

The resistor assembly is mounted in a slightly modified PEBB 1 MCT module housing, sans encasing lid (see Figure 6). The modifications primarily allow for the increased length of the alumina compared to the PEBB 1 aluminum nitride baseplate and the vertical space required for soldering the copper terminals on each end of the resistor. This approach provides an exposed, close to uniform, heating surface that can be viewed from above while the heat sink is mounted below. In addition, by using the MCT module housing, the assembly can be easily mounted to the baffled PEBB 1 heat sink and its derivatives. The Coriolis Corporation curved surface heat sink also has the same screw attachment pattern. Black electrical tape was applied to the inner

^v Hybrid-Tek, Inc., Hytek Corporate Center, Route 526 Millstone Rd. Clarksburg, NJ 08510.

surfaces and on the edges of the opening facing the camera to reduce the reflected infrared from the objects in the background.

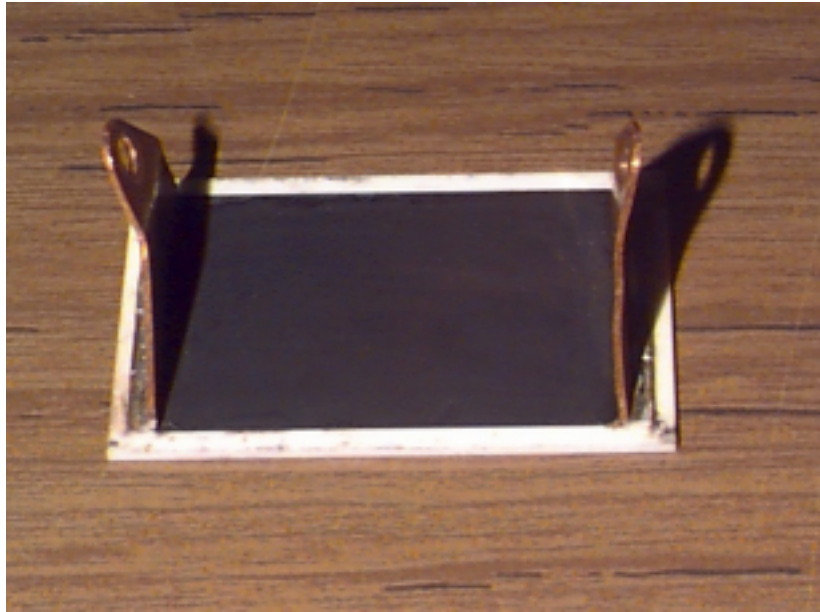


Figure 5. Thick film resistor assembly.

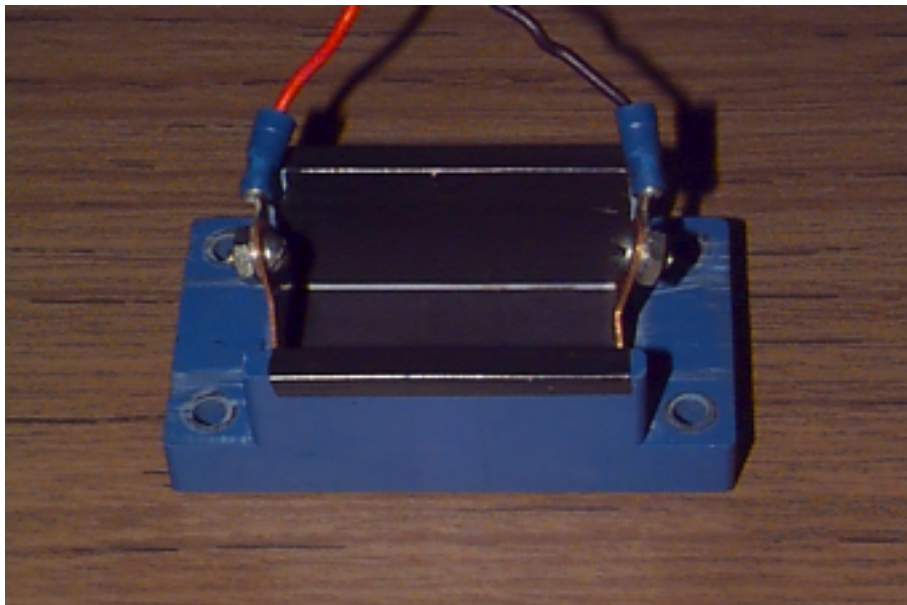


Figure 6. PEBB 1 assembly with PEBB 1 housing.

A few points are in order here concerning the effect that substituting alumina for aluminum nitride will have on the experimental results. The primary change introduced by this substitution is the decrease in thermal conductivity of the resistor substrate (alumina has approximately one-

tenth the thermal conductivity of aluminum nitride). This decrease in thermal conductivity of the substrate will influence the results in a few ways. First, the temperature of the resistor will increase for a given heat generation. This increase in resistor temperature will in turn increase the radiation and convection from the top of the resistor. However, radiation and natural convection from a surface in this temperature range is much less effective in removing heat than forced convection to water. Therefore, these quantities will still be small relative to the heat flux to the heat sink and they will be accounted for as described in the Approach section. The increase in temperature also produces a beneficial effect that more accurate results are obtained with the infrared camera when the temperature of the subject is further from the background temperature.

The decrease in the thermal conductivity of the substrate will also affect the spreading through its thickness. The Biot number is the thermal resistance to heat transfer through the substrate divided by the thermal resistance below the substrate. It can be expressed as

$$Bi = \frac{ht}{k}, \quad (2)$$

where h is an equivalent convection heat transfer coefficient representing all heat dissipating mechanisms below the substrate, t is the substrate thickness, and k is the thermal conductivity of the substrate. An increase in the Biot number leads to a decrease in the amount of thermal spreading through the thickness of the substrate¹. An example that clarifies this inverse relationship would be a substrate with an insulated lower surface, which would give a Biot number of zero. The primary path of the heat generated would then be laterally in the substrate, giving very high spreading. Substituting alumina for aluminum nitride results in an increase in the Biot number and therefore reduced thermal spreading, this in turn would result in better resolution in the thermal impedance results obtained with the infrared camera.

Test instrumentation consists of two pressure gauges, a differential pressure gauge, a flow meter, two thermistor probes and a digital thermometer, an infrared thermal imaging camera, and two digital multimeters. The pressure gauges were used to measure the pressure drop across the test device with the differential gauge being used when pressures exceeded the range of the other gauges. They were installed in the test apparatus supply and return lines. The thermistor probes were also mounted in the supply and return lines to measure the bulk temperature rise of the water through the test device. The flow meter was mounted in the return line to monitor the cooling water flow rate. All TFR temperature measurements were made using an infrared thermal-imaging camera. The current and the voltage drop for the TFR were measured with the digital multimeters to determine the power being dissipated.

Calibration

The data collected for calibration included quantities necessary for determining the emissivity of the TFR material, ϵ , verification of the resistor uniformity, estimation of the radiation and convection heat fluxes from the top of the resistor, and the pressure drop of the test fixture and hoses. The first three measurements were only made once for a particular resistor design, unless significant changes were made to the test setup orientation or ambient conditions that would drastically affect radiation or convection. In such an instance, a second calibration would be made. The measurements made in the cooling water system to account for fixture pressure drop were repeated for each plumbing configuration.

Resistor Emissivity

The emissivity of the resistor material is required as input to the infrared thermal imaging camera (or it can be entered into the Thermonitor Lite^{vi} image processing software) to produce accurate temperature readings. No data on the emissivity was available from the manufacturer of the resistor material; therefore, it was determined experimentally in the calibration phase of this study.

The approach used to determine the resistor emissivity, which can have a value between zero and one, was to use the infrared camera to simultaneously image the resistor with a second material of known emissivity at the same temperature. The thermal image processing software was then used to match the indicated temperature of the two materials using the known emissivity of the second material and varying the emissivity of the resistor. This procedure was then repeated over the range of temperatures to be encountered during testing to characterize the dependence of the resistor's emissivity on temperature.

The reference material used in this test was electrical tape, having a known emissivity of 0.95. The electrical tape was used to attach a thermocouple to the surface of the resistor for monitoring the temperature of both the tape and the resistor during the test (see Figure 7). An oven was used to heat the assembly to a desired temperature, they were removed from the oven, and the infrared image was made before they cooled significantly. They were removed from the oven prior to imaging because if it was done while still in the oven, the background temperature (the temperature inside the oven) and the subject temperature would be the same and the indicated temperature would be nearly independent of the emissivity. To keep the temperature of the assembly from dropping too rapidly while outside of the oven, they were placed on a 1/2 inch plate of aluminum, which was heated and removed with the resistor.

^{vi} Trademark software of Inframetrics Incorporated, 16 Esquire Road, North Billerica, MA 01862

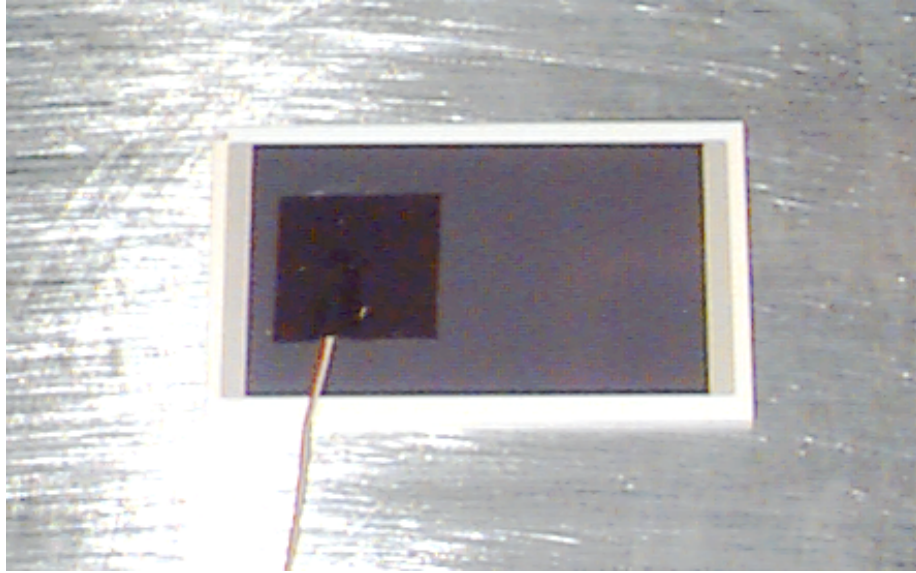


Figure 7. Resistor Emissivity Calibration Test.

The results of this calibration were that the emissivity of the resistor was found to be very stable in the range from 45–100 °C at a value of $\epsilon = 0.70$. This result is very positive because it avoids a significant complication to the data reduction that would be necessary for a material with an emissivity that varies with temperature.

Resistor Uniformity

Determining the uniformity of the TFR is important because the distribution of the heat generated by the resistor is governed by it. A uniform sheet resistivity translates to a uniform heating, which simplifies the data reduction procedure as compared to a non-uniform resistor. The primary factor that will govern the variability of the sheet resistivity is the thickness of the resistor material as it is expected that the composition of the material is uniform over the area.

Determining the uniformity of the resistivity proved to be more difficult than initially expected. The original concept for this test was fairly simple – apply a brief current pulse to the resistor to heat it and record the temperature distribution using the infrared camera before the heat dissipates into the alumina substrate. By using the current pulse, the three-dimensional (3D) steady state thermal conduction into the alumina and from the alumina to objects under it and to the air are not of concern since the heat does not have time to leave the resistor material. In actuality, this approach proved to be a challenge due to difficulties in timing between the current pulse and the recording of the temperature distribution and in the actual capturing of the temperature distribution.

A schematic of the circuit and equipment used in this test is shown in Figure 8. A bank of capacitors charged by a DC power supply acted as the energy source for the current pulses. A Harris PEBB 1 footprint IGBT was used to close the circuit to start the pulse and then open again to complete it. A wave/pulse generator triggered externally by computer provided the signal to the gate driver of the IGBT. A Nicolet digital oscilloscope was used to monitor the signal to the IGBT gate driver as well as the current and voltage of the pulse.

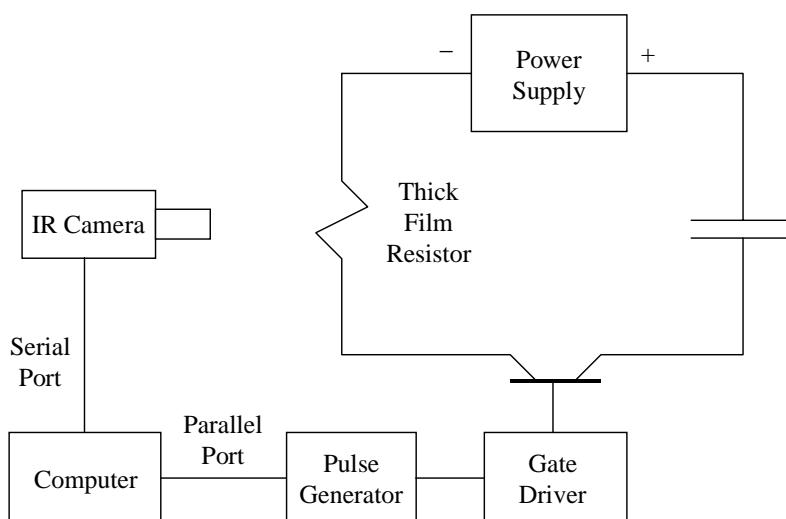


Figure 8. Schematic of resistor uniformity test apparatus.

A laptop computer running National Instruments' LabVIEW software controlled the timing between the current pulse and the recording of the resulting temperature distribution in the resistor. One bit of the parallel port of the computer was used to provide the trigger signal for the wave/pulse generator to start the pulse. The duration of the current pulse was set manually on the front panel of the wave/pulse generator. The infrared thermal imaging camera is controllable by ASCII commands through a serial interface only and LabVIEW was programmed to provide these commands. This reliance on the serial port to initiate the capture of the thermal image proved to be a significant hindrance to this test due to the inconsistent control of timing that results. The length of time between the start of the current pulse and the image capture was impossible to control accurately. However, it was felt that through repeated pulsing an image would eventually be captured at the appropriate time. Unfortunately, a characteristic of the camera in the way images are captured limited the effectiveness of the repetition strategy.

Although the infrared camera used in this test has a focal plane array for infrared detection as opposed to a single sensor with a scanning mirror, it still must pass data from the individual cells in the array to the image processing circuitry. While this occurs much faster than with a scanning mirror, it still takes a couple milliseconds and this is on the order of the time it takes for

the heat generated in the resistor to dissipate to the alumina. Figure 9 contains two images from preliminary testing showing how the results varied from distributions hotter at the top than the bottom to others hotter at the bottom than the top. This difference in temperature distribution results from the relative timing between the pulse and the image capture. If the pulse starts just after the image capture begins, the pixels for which data is processed first are colder and those processed last are hotter. If relative timing is such that the pulse ends before the image is completely captured, the pixels processed first are hotter than those processed last and the opposite temperature distribution is seen. It was verified that this was what was happening rather than a physical phenomenon with the resistor by rotating the camera 90° with respect to the resistor and seeing the patterns rotate as well (see Figure 10).

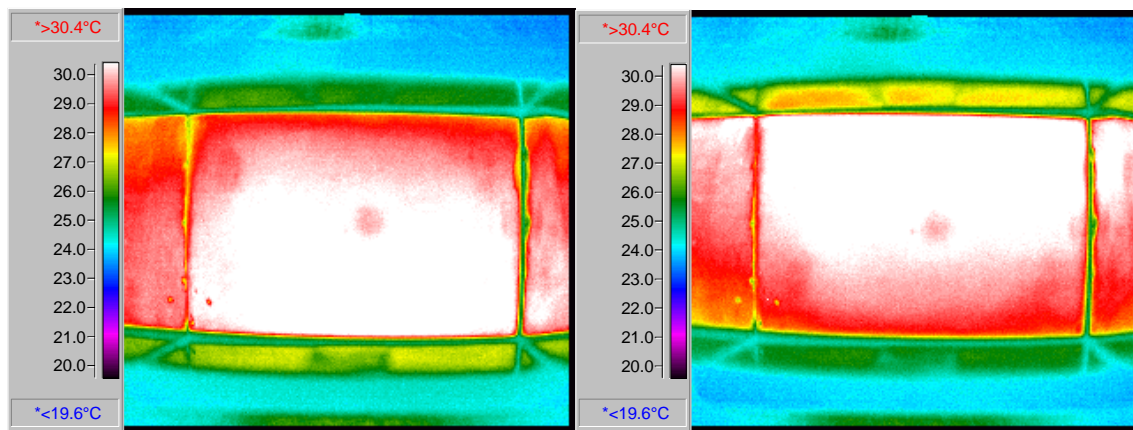


Figure 9. Sample thermal images showing varying results from uniformity pulse testing (spot in center is reflection of camera lens)

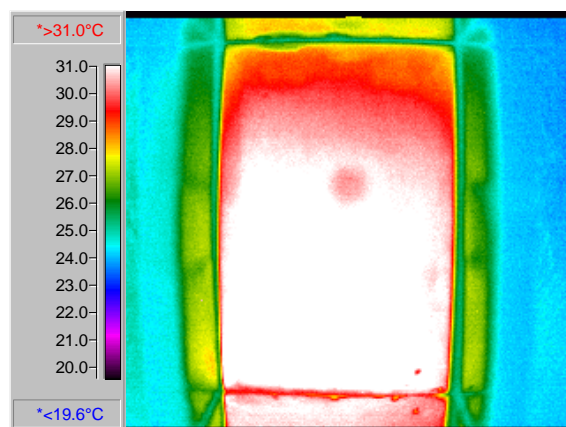


Figure 10. Sample thermal image from uniformity pulse testing with camera rotated 90° (spot in center is reflection of camera lens).

While the difficulties mentioned here prevented obtaining 100% conclusive results regarding the uniformity of the resistors, examination of several of them did give a confidence level sufficient to continue with this approach. For instance, uniformity from side to side (along a horizontal scan) for a resistor was observable and rotating the camera 90° allowed observation in the orthogonal direction. In addition, the pulse testing was repeated several times until images were captured that had relatively good symmetry from the top to the bottom of the image. Although the exact timing between the pulse and the capture for these images is not known, they do provide useful results.

Figure 11 is an example of an image that appears to have been captured at an optimal time relative to the heating pulse. Although steps were taken to reduce reflections off the resistor from objects in the room, the fact that the resistor was typically only about ten degrees above ambient made any reflection significant. To correct for these reflections, the image shown in Figure 12 was taken of the TFR at room temperature to act as a baseline for determining the temperature rise produced by the pulses. By subtracting the baseline distribution in Figure 12 from the results in Figure 11, the temperature rise was determined for the resistor portion of the image and is shown in Figure 13. This graph shows that except for the very edge of the resistor, uniformity in the sheet resistivity appears to be good. The data reduction will account for this apparent non-uniformity near the resistor edges by cropping that area out of the analyzed part of the resistor. It should be noted that the denominator of equation (1) will still be determined based on the total area of the resistor. Therefore, if the sheet resistivity is lower near the edges, the actual value of $(q/A)_{sink}$ in the analyzed region will be larger than calculated and the resulting resistor thermal impedance $\theta_{TFR}(x, y)$ will be higher than actual and conservative from the designer's perspective.

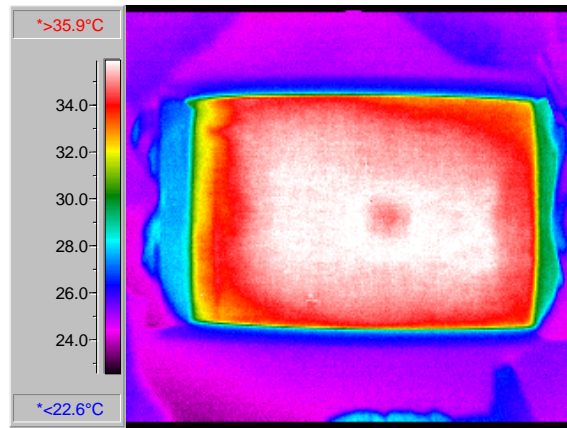


Figure 11. Uniformity pulse testing image.

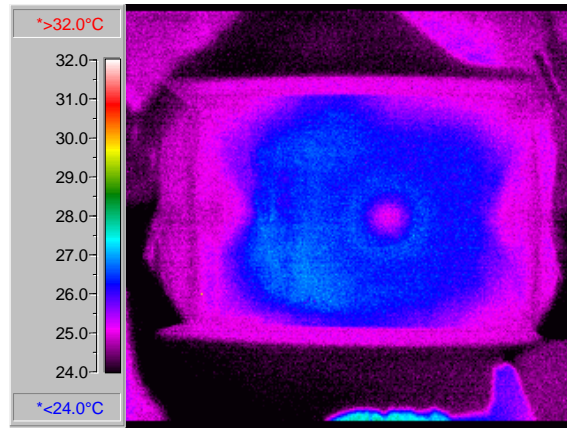


Figure 12. Image of unheated TFR showing infrared reflections.

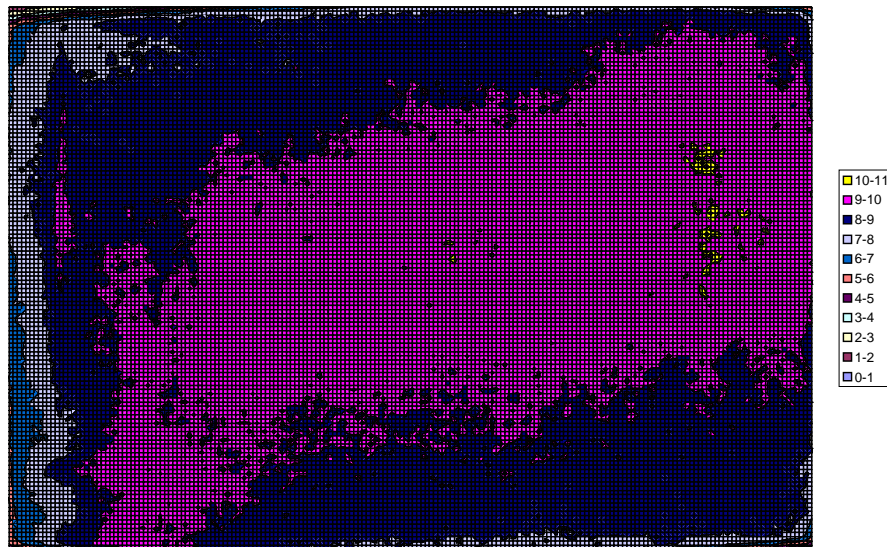


Figure 13. Graph showing uniformity pulse test results.

Radiated and Convected Heat Flux

The radiated and naturally convected heat flux values from the top of the TFR are used in the calculation of the heat flux to the heat sink. It should be noted that analytical expressions approximating these quantities can be determined; however, because their magnitude is small compared to the heat flux to the heat sink and accurately determining coefficients in these expressions can be involved, the approach described below was used.

The approach used was to pass current through the resistor to heat it, measure the temperature of its surface, and determine the radiated and convected heat transfer rate per unit

area for that temperature. The temperature of the surface of the resistor was measured with the infrared camera. The heat flux from the top of the resistor was determined through an energy balance between heat generated and heat dissipated. The bottom of the resistor substrate was insulated in order to minimize the heat conducted through the substrate and into the surroundings underneath the resistor. The heat dissipated from the top of the resistor via convection and radiation is given by the following expression:

$$(q/A)_{rad+conv} = (q/A)_{heating} - (q/A)_{sink} . \quad (3)$$

The heat transfer rate per unit area generated through resistive heating was calculated by dividing the electric power being dissipated from the resistor by its area. The amount of heat escaping through the insulation is very small and was neglected.

The procedure used for determining the radiated and convected heat fluxes was as follows:

1. Insulate the bottom of the TFR substrate with the resistor mounted in the PEBB 1 housing. Dow Trymer 1800™ polyisocyanurate foam insulation, which is rated to 149 °C, was used.
2. With the infrared camera pointed at the assembly, apply a voltage sufficient to reach an approximate steady-state average temperature of 30 °C.
3. Save the thermal image to a file for determining the actual average temperature using data analysis software. Record the voltage and current applied to the resistor.
4. Increase the voltage to the resistor sufficiently to increase the average temperature by 10 °C.
5. Repeat steps 3 and 4 until a temperature of 120 °C is reached.

A plot of radiated and convected heat flux area versus resistor surface temperature is shown in Figure 14. These results are very linear in this temperature region and a straight-line curve fit was made for use in reducing the experimental data from heat sink testing.

Fixture Pressure Drop

Because of the difficulty in mounting pressure gauges in the test apparatus in a way such that they measure only the pressure drop across the heat sink, calibrations were made to account for fixture pressure drop between the pressure ports and the heat sinks. A compensation curve for each test configuration was determined by measuring the pressure drop without a heat sink installed. A piece of tubing equal in length to the two pieces used with the heat sink was substituted. The circulating pump was turned on and the flow rate through the tubing was varied. Pressure drop readings were made at 0.5 gpm increments up to the maximum anticipated for the testing of the particular heat sink. These pressure differentials recorded were due to the test

fixture pressure drop at that flow rate and are subtracted from the Δp measured during heat sink testing. As would be expected for a fluid flow problem, the calibration curves were close to parabolic and were fit very well by a quadratic polynomial.

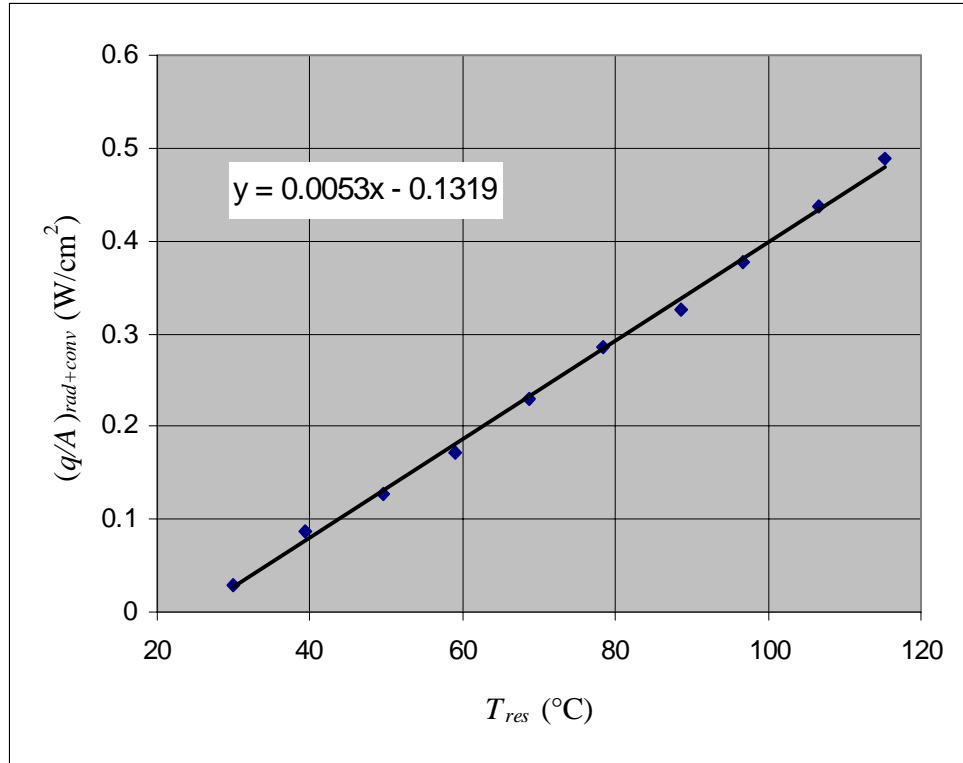


Figure 14. Radiated and convected heat loss from the top of the TFR vs. surface temperature.

Test Procedure

The heat sink experimental performance evaluation is being broken down into two primary areas. The first focuses on the cooling performance of the heat sink as represented by the thermal impedance and the second characterizes the heat sink from the systems perspective, providing pressure drop versus flow rate curves. The experimental measurements for these two areas were recorded simultaneously. This section summarizes the procedures used in collecting the data.

Thermal Impedance

The thermal impedance evaluation was conducted over a range of flow rates and device power dissipation levels. Data taken was used in the calculation of the heat sink thermal impedance distribution and its dependence on the cooling water supply properties. Setup for conducting the thermal impedance testing involved mounting the resistor/heat sink assembly in

the test area and connecting this assembly to the power supply and cooling water. The infrared camera and stand were then positioned above the test assembly and the distance from the camera to the surface of the resistor was carefully set so that it did not vary between tests. Care was also taken to properly center the camera above the resistor and to make certain that the optical axis was normal to its surface.

The following parameters were recorded at each operating state (the associated instrument is listed in parentheses):

- Input water temperature, T_{in} (or T_F) (digital thermistor thermometer)
- Output water temperature, T_{out} (digital thermistor thermometer)
- Water flow rate, Q (flow meter)
- Input water pressure, p_{in} (pressure gauge)
- Output pressure, p_{out} (pressure gauge)
- Differential pressure, Δp_{gauge} (differential pressure gauge)
- Voltage across the resistor, V_{res} (digital multimeter)
- Current through the resistor, I_{res} (digital multimeter)
- Temperature profile across the resistor (infrared camera)

The cooling water temperature was maintained at approximately 20 °C. Original plans called for varying the cooling water temperature, but this was considered unnecessary and was dropped to streamline the testing. The cooling water flow rate was varied from 0.5 gpm up to 3.5 gpm, the maximum that the circulating pump can provide. The voltage and current values were varied based on the electrical power to be supplied to the resistor. The power supplied to the resistor ranged from zero to the maximum that the power supply could supply or the power level that produced a resistor temperature of 100 °C, whichever was reached first. For the 12.5 Ω TFRs used, the maximum power was approximately 1000 W.

External Systems Requirements

The external systems requirements that are of primary concern to system engineers are the flow rate and temperature of water required for cooling and the pressure drop that must be overcome to produce the required flow. These quantities determine the logistics and cost of supplying the cooling water. The cooling water temperature and flow rate and the thermal impedance required are interrelated for a configuration and power level. For a given power level, a lower cooling water temperature would allow a higher thermal impedance, which in turn would allow a lower flow rate. A lower flow rate requires less pumping power; however, cold water may require power for a chiller. Using the data obtained in this experimental program, the

systems designer can make a trade-off between the cooling water flow rate and temperature to choose the best combination for a given application.

The measurements needed for the external systems requirements were made during the thermal impedance testing. At each test condition, the flow rate and corresponding pressure drop was recorded. The pressure drop was determined by subtracting the return pressure from the supply pressure and/or reading the differential pressure gauge and then correcting for the test fixture pressure drop for that flow rate. This procedure makes the assumption that the supply side fixture pressure drop does not depend upon the downstream pressure. Because water is essentially incompressible, this should be a good assumption. The flow rate will be used directly as recorded.

Data Reduction

The calculations used in determining the thermal impedance distribution of the heat sink from the TFR temperature data are presented here. Repeating equation (1) here for convenience, the expression for the thermal impedance is

$$\theta_{sink}(x, y) = \frac{T(x, y) - T_F}{(q/A)_{sink}(x, y)}, \quad (1)$$

where $T(x, y)$ is the temperature distribution over the heat sink interface with the heat source, T_F is the inlet temperature of the cooling fluid, and $(q/A)_{sink}(x, y)$ is the heat transfer rate per unit area through the interface. For a uniformly deposited TFR, the resistive heat generated is uniformly distributed. Assuming the radiation and convection losses from the top surface of the resistor are also uniformly distributed, the heat flux term $(q/A)_{sink}(x, y)$ is constant over the surface and will henceforth be denoted as $(q/A)_{sink}$. This quantity is determined with the expression

$$(q/A)_{sink} = (q/A)_{heating} - (q/A)_{rad+conv} \quad (4)$$

where

$$(q/A)_{heating} = \frac{VI}{A} \quad (5)$$

is the heat transfer rate per unit area generated by the TFR and $(q/A)_{rad+conv}$ is the radiated and convected heat transfer rate per unit area from the top of the resistor. The procedure for determining $(q/A)_{rad+conv}$ was presented in the calibration section along with the resulting curve and curve fit of $(q/A)_{rad+conv}$ versus average surface temperature.

Equation (1) can be rewritten as:

$$\theta_{sink}(x, y) = \frac{T_{TFR}(x, y) - T_F}{(q/A)_{sink}} - \frac{T_{TFR}(x, y) - T(x, y)}{(q/A)_{sink}} \quad (6)$$

where $T_{TFR}(x, y)$ is the temperature of the surface of the TFR. This expression can be summarized as

$$\theta_{sink}(x, y) = \theta_{TOT}(x, y) - \theta_{TFR}(x, y) \quad (7)$$

where

$$\theta_{TOT}(x, y) = \frac{T_{TFR}(x, y) - T_F}{(q/A)_{sink}} \quad (8)$$

is the total thermal impedance from the top of the TFR to the cooling fluid and $\theta_{TFR}(x, y)$ is the thermal impedance of the TFR/substrate combination. For materials with a linear variation of thermal conductivity with temperature, $\theta_{TFR}(x, y)$ can also be determined using properties of the thermal package with the expression

$$\theta_{TFR}(x, y) = \sum \left(\frac{t}{k(1/2(T_1 + T_2))} \right) \quad (9)$$

where t is the thickness of a layer in the package, $k(1/2(T_1 + T_2))$ is the thermal conductivity at the average temperature of the two interfaces of the layer, and the sum is over the different materials through the thickness. Note that k is an indirect function of location in this expression due to the variation of temperature across the resistor.

The summation in equation (9) would normally be taken over all the layers in a package of different materials. In the present case, that would include the resistor material, the alumina, and the PtPdAg metalization. However, the thickness of the resistor and metalization layers relative to the thickness of the alumina allow a simpler approach without introducing significant errors. Both the resistor and the metalization are 12.5 μm (0.5 mil) thick. Although values for the thermal conductivity of the two materials are not known, it is estimated that the resistor material has a comparable k to alumina and that the PtPdAg is at least five times as thermally conductive. This combination of small thickness relative to the alumina (less than 1%) and comparable or higher thermal conductivities allows these layers to be neglected in determining $\theta_{TFR}(x, y)$ with less than 1% error introduced. Even if the resistor material possesses a k significantly larger than alumina, the fact that it is the layer in which the heat is generated would offset the effect of that on $\theta_{TFR}(x, y)$.

Point-wise values for the distribution of $\theta_{TOT}(x, y)$ and $\theta_{TFR}(x, y)$ are determined separately in an Excel spreadsheet and subtracted to yield $\theta_{sink}(x, y)$. First, $(q/A)_{sink}$ is calculated by substituting equation (5) into equation (4) along with the expression from the curve fit to experimental data shown in Figure 14 for the radiated and convected heat loss from the top of the resistor. Using the resistor area of 16.7 cm^2 yields

$$(q/A)_{sink} = \frac{VI}{16.7 \text{ cm}^2} - (5.3 \times 10^{-3} \text{ W / cm}^2 \cdot ^\circ\text{C})T_{res} + 0.13 \text{ W / cm}^2. \quad (10)$$

Where VI is the electrical power being dissipated by the resistor and T_{res} is the temperature of the TFR surface. The average temperature of the resistor is used for T_{res} in this study. $\theta_{TOT}(x, y)$ is calculated using equation (8), the results from equation (10), the cooling fluid temperature, and the infrared camera temperature data, which is exported as pixel-wise ASCII data from the Thermonitor Lite software purchased with the camera.

Calculation of $\theta_{TFR}(x, y)$ using equation (9) will utilize the temperature data from the infrared camera and heat transfer rate per unit area from equation (10) to determine the average temperature and hence the thermal conductivity of the alumina. Using the notation introduced previously for the temperature at the bottom of the alumina, $T(x, y)$, the average temperature of the alumina is expressed as

$$T_{AL} = 1/2 [T_{TFR}(x, y) + T(x, y)]. \quad (11)$$

With the introduction of $\Delta T = T_{TFR}(x, y) - T(x, y)$, equation (11) can be rewritten as

$$T_{AL} = T_{TFR}(x, y) - 1/2 \Delta T. \quad (12)$$

Using Fourier's heat conduction law,

$$\Delta T = (q/A)_{sink} \frac{t}{k}, \quad (13)$$

the alumina's thickness of 0.15 cm, and an average value for k in the temperature range from 20 to 100 $^\circ\text{C}$ of 0.22 W/cm- $^\circ\text{C}$ (see Figure 15), the resulting expression for the approximate average temperature of the alumina is

$$T_{AL} = T_{TFR}(x, y) - (0.34 \text{ } ^\circ\text{C} \cdot \text{cm}^2 / \text{W})(q/A)_{sink}. \quad (14)$$

The thermal conductivity in equation (13) has a second order influence on the thermal impedance and only varies by $\pm 14\%$ from 0.22 in the temperature range of concern and therefore its variation with temperature was not included here. Errors in determining k in this manner were verified to be less than 1% when compared to a more rigorous approach that accounted for a

nonlinear temperature variation through the thickness. Substituting the linear approximation to the curve fit in the same 20 to 100 °C range of Figure 15 into equation (9) yields

$$\theta_{TFR}(x, y) = \frac{0.15}{-8 \times 10^{-4} T_{AL} + 0.28} \text{ } ^\circ\text{C}\cdot\text{cm}^2/\text{W} \quad (15)$$

for T_{AL} in °C.

The calculation of the distribution of the thermal impedance $\theta_{sink}(x, y)$ using equations (7), (8), and (15) was repeated for each resistor dissipation power level and at each flow rate. In addition, the average value of the thermal impedance over the area and the standard deviation of the distribution were calculated. These two values provide the basis for a quantitative comparison of the performance of different heat sink designs in terms of their overall cooling capability and the uniformity of that cooling.

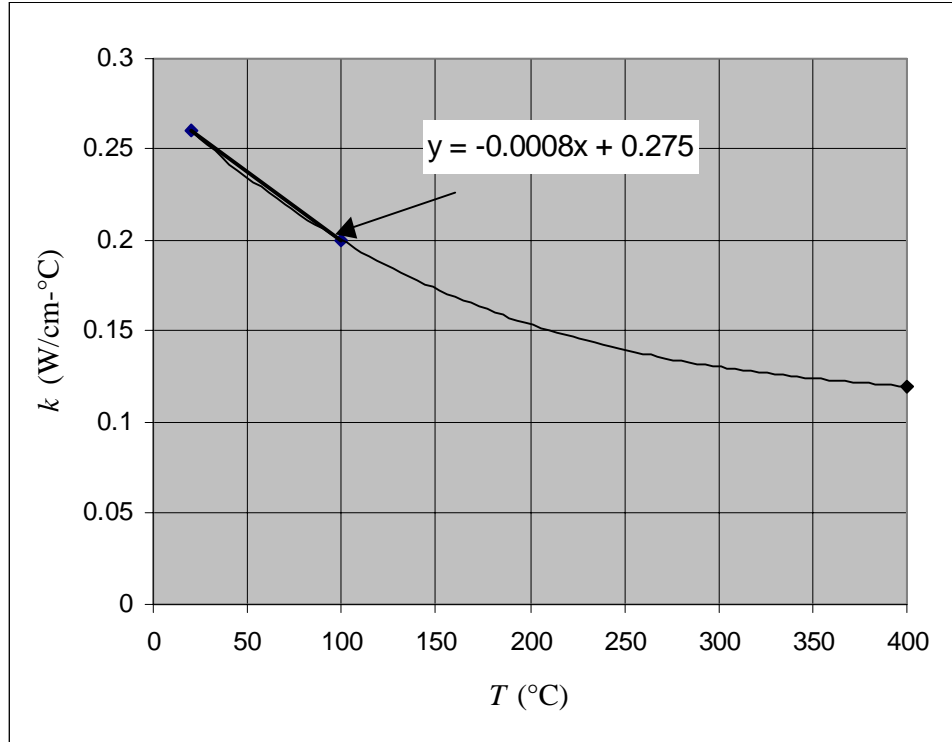


Figure 15. Thermal conductivity vs. temperature for 96% alumina.^{vii}

^{vii} Data for Coors ADS-96R.

PRELIMINARY RESULTS

Results contained in this report were obtained during calendar year (CY) 98. The data has been reduced using the expressions presented in the Approach section and some comparisons have been made between different heat sinks. Additional analysis of the data will be completed in CY99 along with the evaluation of other concepts and comparison to analytical results.

Baseline Heat Sink

The baseline heat sink was a simple open chambered design derived from the original PEBB 1 baffled heat sink. Shown in Figure 16, it was created by removing the baffles and adding output ports to the opposite side of the PEBB 1 heat sink across from the two existing ports. The objective was to create a heat sink for which developing an analytical approximation would be easier than for the baffled design and therefore potentially makes a useful baseline case.



Figure 16. Baseline heat sink.

The heat sink was connected to the test apparatus through a pair of short 1/4" ID Tygon® tubing at each end connected to a pair of short pieces of 3/8" Tygon® tube by reducers that were then joined together with a "Y" coupling to a single 3/8" tube. This configuration was used in order to minimize the pressure drop of the connections by using 3/8" tubing as opposed to 1/4" as much as possible. Without taking these steps, the pump was only able to produce 3 gpm of flow. With these modifications, 3.4 gpm was reached.

Testing of the open chambered heat sink was the first use of the VECTOR thermal management testing facility and was therefore partially a learning experience. Test procedures were refined during this phase of testing and data reduction procedures and routines were

developed and refined. It was also determined that this particular configuration of open chambered heat sink was probably not the best option, primarily due to the inlet and outlet ports. The use of two small fittings introduced uncertainty in the character of the flow in the chamber and significant variability was observed when the supply and return tubing were moved during testing. An alternative open chambered configuration is planned for future testing, however, the results from this series of tests is presented here for reference and discussion.

Thermal Impedance

One of the refinements that was added as a result of observations during these tests was the use of two thermal images in performing the data reduction. Figure 17 contains two infrared thermal images captured at the same operating condition for the open chambered sink, but at different times only a second or two apart. The slight differences between the two images reflect the unsteady character of the coolant flow through the chamber. While the testing was being done, the temperature distribution was observed to vary in an irregular manner. This unsteady nature was probably due to a fluid dynamic phenomenon such as vortex shedding at the inlet ports. The two temperature distributions captured were averaged during data reduction to lessen the effect that the unsteadiness would have on the trends observed.

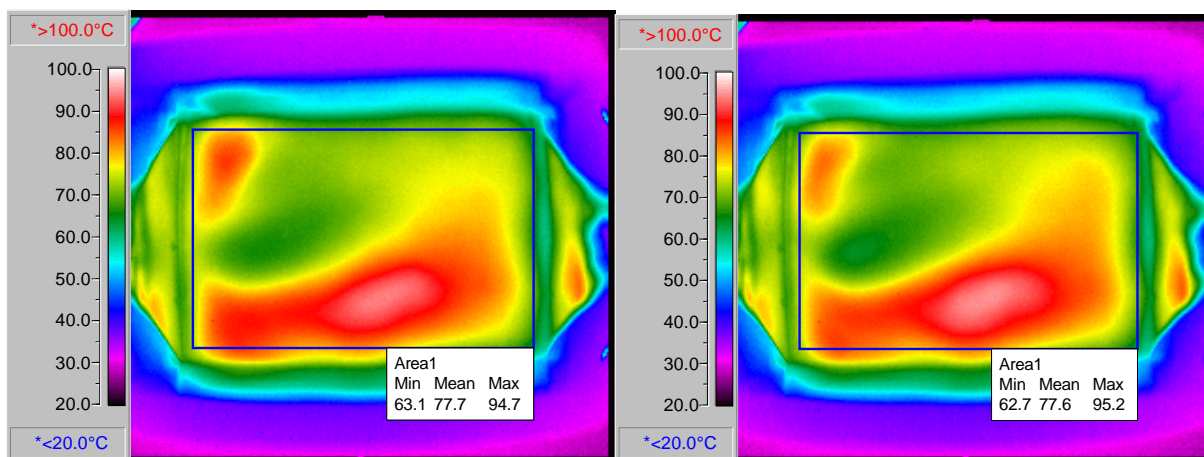


Figure 17. Two open chambered heat sink temperature distributions at 0.5 gpm flow rate and 400 W dissipation taken moments apart.

The rectangular boxes shown in each image labeled “Area1” are selection areas for the data analysis. Each pixel in these rectangles has a temperature value associated with it that is exported to MS Excel for data reduction and analysis. The label box for these rectangles also displays the minimum, mean, and maximum temperature within the rectangle and gives a quantified indication of the unsteadiness.

Pairs of images such as those in Figure 17 were captured at each operating condition for all of the heat sinks included in this report, however, for the sake of brevity only one of the pair will typically be included. Figure 18 is a thermal image for the 3.4 gpm flow rate, 800 W dissipation operating condition. While the temperature distribution pattern is very similar to that from the 0.5 gpm flow rate, the range of temperatures within the rectangle is narrower due to improved mixing. In addition, for twice the power level being dissipated, the temperatures in Figure 18 are less than those in Figure 17, indicating a significant reduction in thermal impedance with increased flow rate.

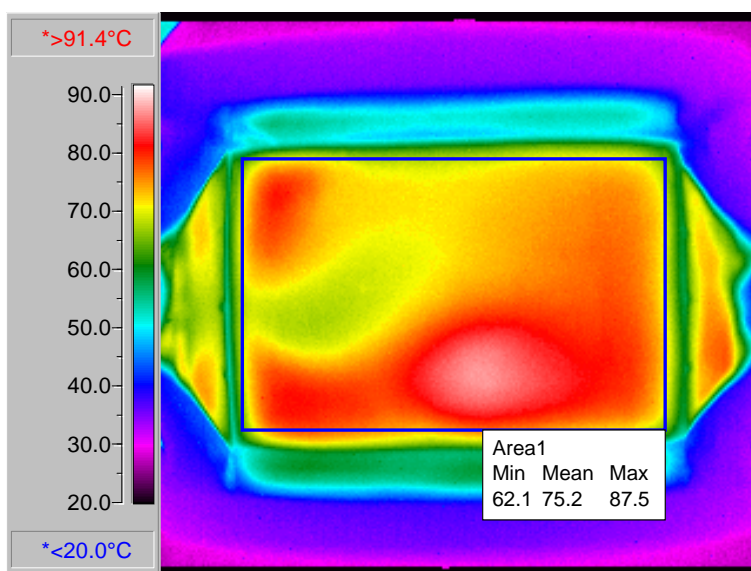


Figure 18. Open chambered heat sink temperature distribution at 3.4 gpm flow rate and 800 W dissipation.

Figure 19 is a plot of the average thermal impedance versus heat flux density for the five flow rates tested. The difference in the maximum heat flux density reached for each flow rate is due to the limit placed on the maximum temperature of the resistor. As stated previously, this limit was set at 100 °C to avoid cracking the alumina substrate from local boiling. Because the thermal impedance is higher at lower flow rates, the maximum heat flux density achievable under this limit is lower.

The decline in the curves in Figure 19 as the heat flux density increases is not as easy to explain. Two possible causes for this are hypothesized, however neither has been proven to be a contributor. The first possible cause is a form of measurement error in the use of the infrared thermal imaging camera. In order for the camera to provide accurate readings, two pieces of information must be supplied: the emissivity of the surface of the object and some way of determining the infrared energy incident on the object. For something opaque to infrared, such as

the TFR, infrared coming from its surface is either emitted due to its temperature or reflected from infrared incident upon its surface. By supplying the infrared camera or image processing software with the emissivity of the object and the background temperature, a good estimate of these quantities and therefore the object's temperature can be made. However, errors in determining the incident infrared can produce errors in the temperature estimates that are more significant at temperatures close to the background than at higher temperatures. If this estimate of the incident infrared is lower than the actual, the excess will be attributed to the temperature of the subject and a temperature reading higher than actual will result. This error will be constant with subject temperature and would therefore be less significant in calculating the thermal impedance at higher temperatures. For an underestimation error in the TFR temperature, the result would be the type of curves seen in Figure 19.

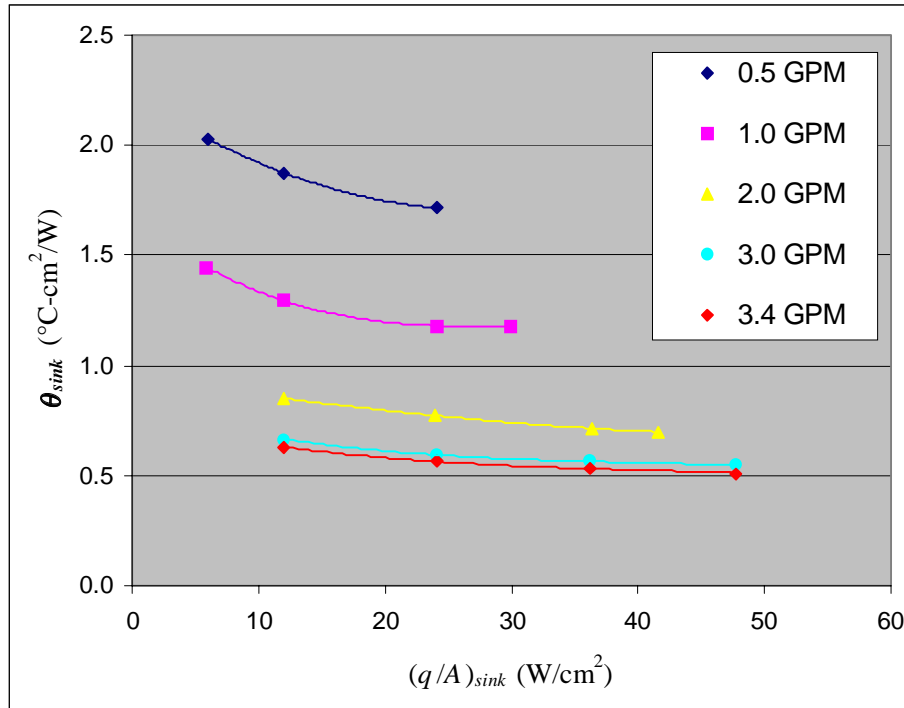


Figure 19. Open chambered heat sink average thermal impedance vs. heat flux density.

The second hypothesized source for the declining curves in Figure 19 is that the variation in the cooling water properties with temperature is influencing the convection heat transfer. Moving from left to right for each curve in Figure 19, the temperature of the resistor is increasing, as is the temperature of the bottom of the resistor substrate in contact with the cooling water, denoted $T(x, y)$. This temperature is typically labeled T_{wall} in boundary layer analysis. In convection heat transfer analysis, the empirical relation between the film coefficient, h , and the Reynolds and Prandtl numbers for laminar flow over a flat plate is of the form $h = f(\text{Re}^{1/2} \cdot \text{Pr}^{1/3})$. The

property of water most heavily influenced by temperature is the viscosity, which decreases with increasing temperature. The Reynolds number is inversely proportional to the viscosity while the Prandtl number is directly proportional. Therefore, because the film coefficient is influenced to a higher order by the Reynolds number than the Prandtl number, the net effect of a decrease in viscosity is an increase in the film coefficient, which corresponds to a decrease in the thermal impedance.

It is likely that both of these hypothesized causes are present to some degree and the relative influence of them will be examined further in the final report. In order to minimize the influence of infrared measurement error in comparing the different heat sinks, the thermal impedance used in such comparisons will be for the highest heat flux test cases when possible.

Figure 20 is a plot of the average thermal impedance versus cooling water flow rate for the highest heat fluxes reached at each flow rate. These data points correspond to the points at the right-hand end of the curves in Figure 19. From this plot, it appears that increasing the flow rate beyond the 3.4 gpm maximum tested here will continue to improve the thermal performance, however, it is not clear whether the potential gains would be worth the increase in pumping power required.

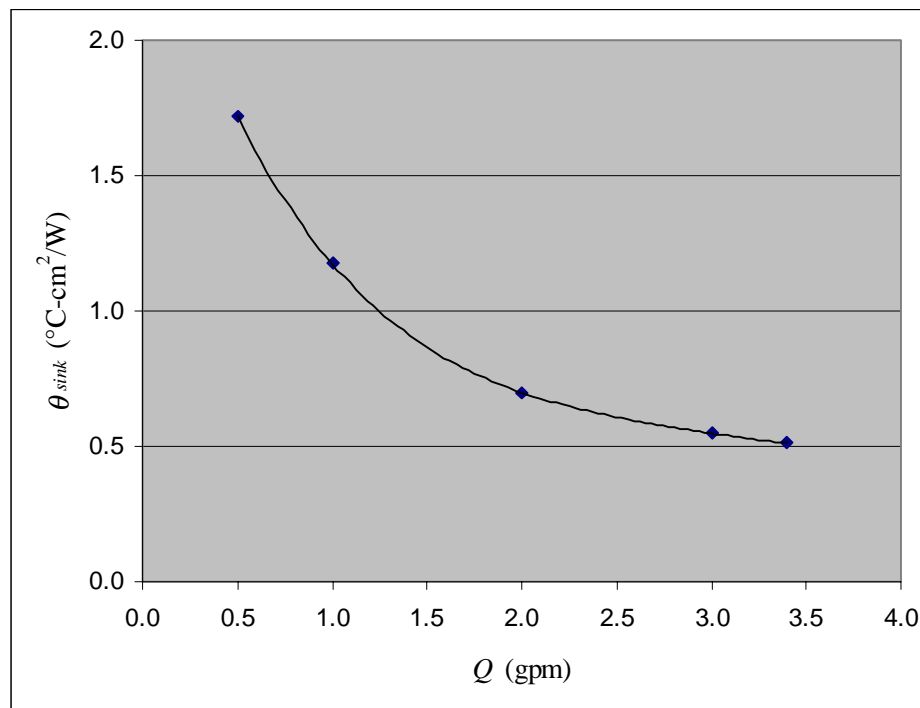


Figure 20. Open chambered heat sink average thermal impedance vs. coolant flow rate.

The standard deviation of the thermal impedance distribution is a quantitative measure of the uniformity of the cooling provided by the heat sink. Figure 21 is a plot of the thermal impedance standard deviation versus flow rate for the open chambered heat sink. The shape of this curve is very similar to the thermal impedance curve of Figure 20 with the poorest performance occurring at the lower flow rates. As with the thermal impedance, the maximum flow rate tested, 3.4 gpm, appears to be near the point of diminishing returns. While the standard deviation is useful in providing a measure of the heat sink's uniformity, it is still important to examine the thermal impedance distribution as represented by the thermal images of Figure 17 and Figure 18. From these images, the locations of the hot areas can be seen and improvements can be made or the semiconductor dies can be placed in such a way as to avoid them.

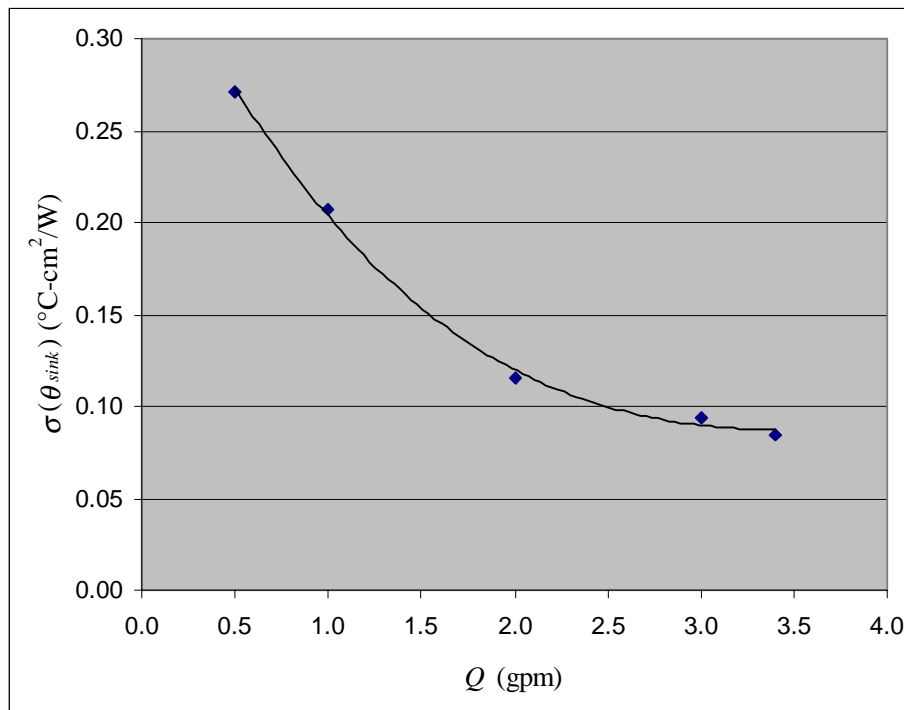


Figure 21. Open chambered heat sink thermal impedance standard deviation vs. flow rate.

External System Requirements

Typically, for a heat sink with as little to impede coolant flow as an open chambered heat sink, the pressure drop through it would be very low. However, the use of 1/4" barbed hose fittings on this heat sink introduced a significant pressure drop that can be seen in the plot of pressure drop versus flow rate in Figure 22. The inside diameter of these brass fittings was approximately 3/16" and the openings had square edges, which further increased the pressure

drop. This aspect of the open chambered heat sink also points toward the use of a better baseline, which as stated earlier, is planned for future tests.

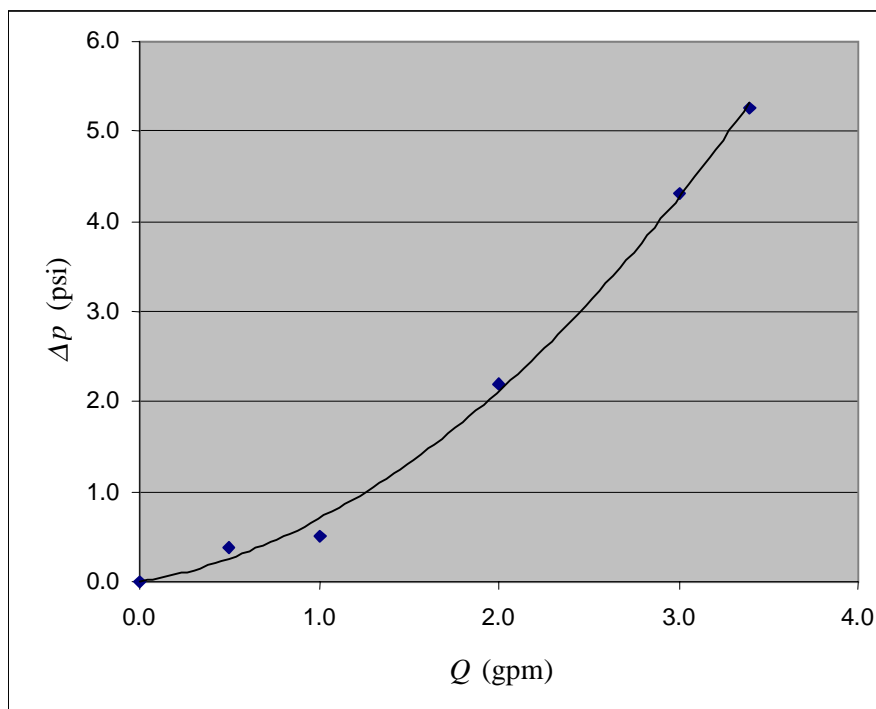


Figure 22. Pressure drop vs. flow rate for open chambered heat sink.

Harris PEBB 1 Baffled

Harris developed this baffled heat sink for use in liquid cooling their PEBB 1 modules. Figure 23 is a photograph of this heat sink showing the fluid input and output located on the same side of the chamber with partitions and pins molded into the plastic to channel the flow over the entire baseplate of the module and to enhance mixing and turbulence. While in concept this sounds like a reasonable approach, there are significant shortcomings to its implementation that will become very evident through the testing done for this report.

This heat sink was connected to the cooling water system with 1/4" Tygon® tubing at each fitting. Because there was only one inlet and one outlet port on this heat sink, twice the flow rate was present in each of these passages as compared to the open chambered heat sink. In combination with the serpentine passage within the heat sink, this produced significantly higher pressure drops and limited the maximum flow rate that could be achieved with the pump to 3.0 gpm.

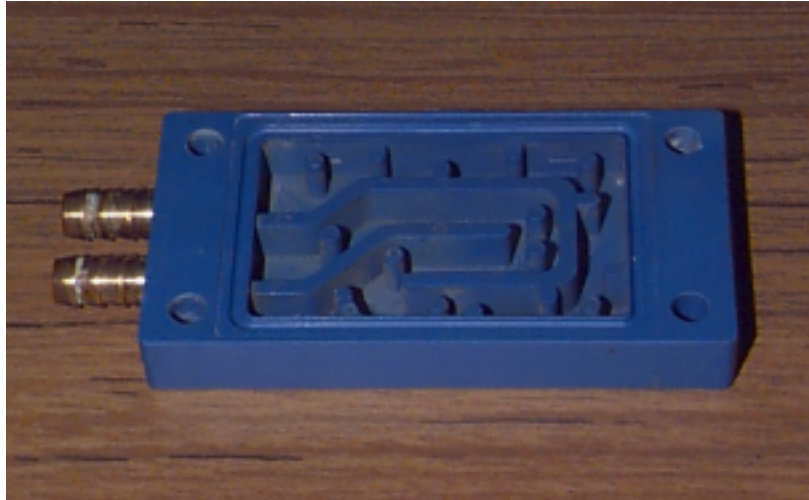


Figure 23. Harris PEBB 1 baffled heat sink.

Thermal Impedance

As with the open chambered baseline heat sink, temperature distributions were captured in pairs at each operating condition and averaged to determine the thermal impedance. Figure 24 shows both the temperature distribution for the 3.0 gpm, 1 kW operating condition and a picture of the heat sink in the same orientation as was used in the test, with the flow direction labeled. It is clear from the image that this heat sink provides fairly nonuniform cooling with the most effective occurring very close to the inlet port. The rest of the heat sink apparently does not see as much of the coolant flow as that region does. It was decided that the likely cause of this was the approximately 0.035" gap between the top of the partitions and the TFR baseplate allowing a significant portion of the flow to bypass the rest of the passages. The modified Harris PEBB 1 heat sink addressed this shortcoming by increasing the height of the partitions to determine how much improvement this could provide.

During PEBB 1 testing by NSWCC, a thin aluminum plate holding five thermocouples was inserted between the module baseplates and heat sinks. One of these thermocouples was located at the center of the baseplate and the other four were placed at the center of each quadrant of the baseplate, forming a pattern like that of the five spots on a game dice. Comparison of NSWCCD's data to the cooling distribution seen here, the thermocouple measuring the highest temperature was located in the region of highest thermal impedance. This provided confidence in these results and indicated that the poor uniformity seen here could have been a contributing factor to some of the failures seen during these tests.

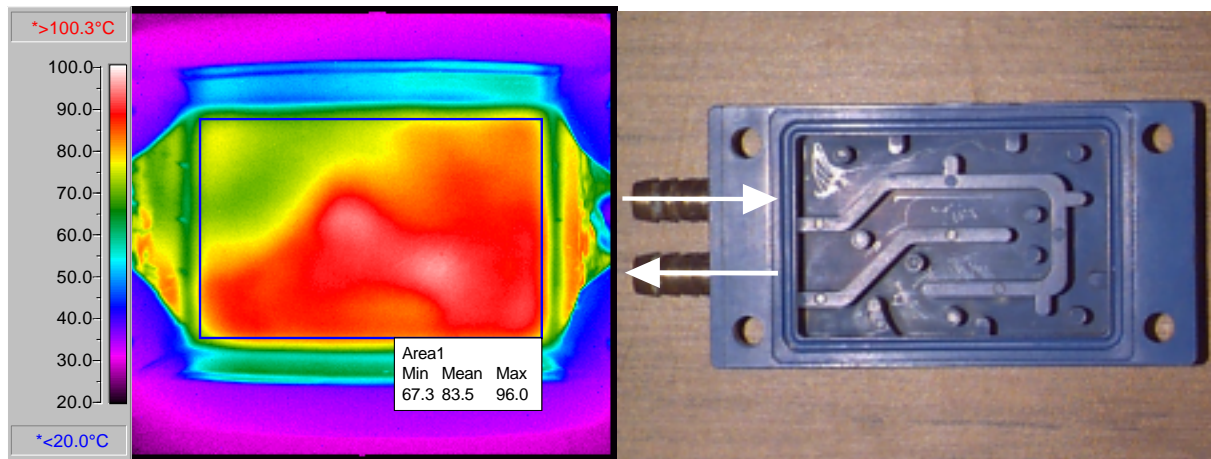


Figure 24. Harris PEBB 1 heat sink temperature distribution at 3.0 gpm flow rate and 1.0 kW dissipation.

Figure 25 is the plot of average thermal impedance versus heat flux density for the four flow rates tested. As with the open chambered baseline heat sink, these curves decline with increasing heat flux density. Due to the improvement in thermal impedance over that seen with the open chambered baseline, a resistor power of 1.0 kW was reached in these tests within the imposed maximum resistor temperature of 100 °C. While pressure drops were significantly higher for this heat sink, its performance at 3.0 gpm was approximately 20% better than the baseline at 3.4 gpm. These results are consistent with what would be expected for flows at a higher velocity, which is the case here due to the smaller cross sectional areas of the passages in the PEBB 1 heat sink.

Figure 26 plots the average thermal impedance versus cooling water flow rate for the highest heat fluxes reached at each flow rate. The shape of this curve is very similar to the same plot for the open chambered baseline heat sink. The thermal impedance standard deviation versus cooling water flow rate is shown in Figure 27. While the average thermal impedance improved relative to the baseline open chambered heat sink, the standard deviation of the thermal impedance remained about the same. This is due to the bypassing of a significant portion of the flow over the top of the partitions producing a large area of poor cooling. As a percentage of the overall average thermal impedance, this value of the standard deviation corresponds to about 24% versus about 17% for the baseline, a moderately poorer result.

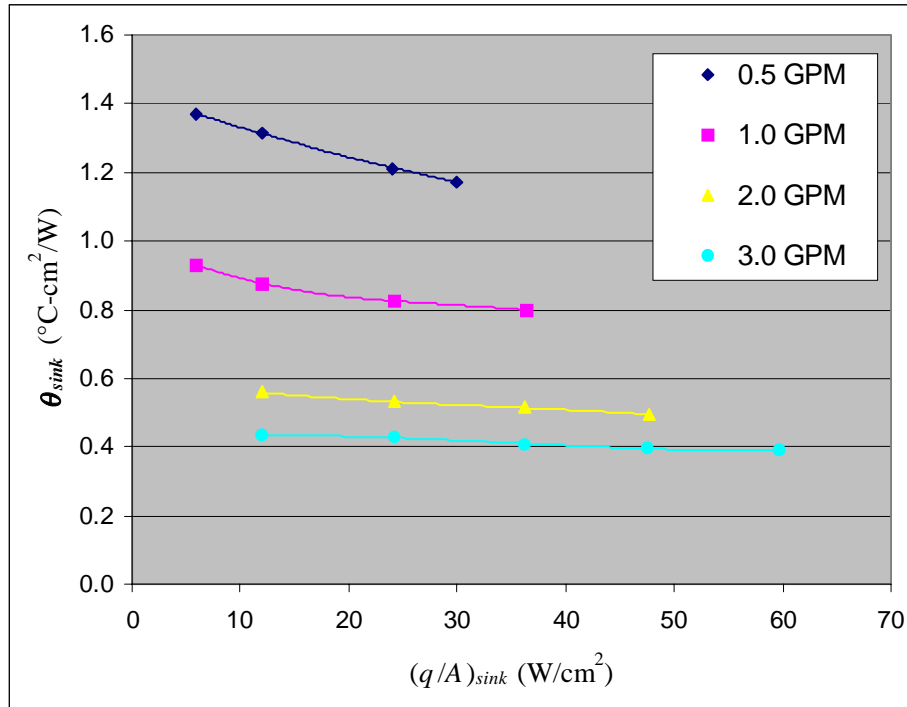


Figure 25. Harris PEBB 1 heat sink average thermal impedance vs. heat flux density.

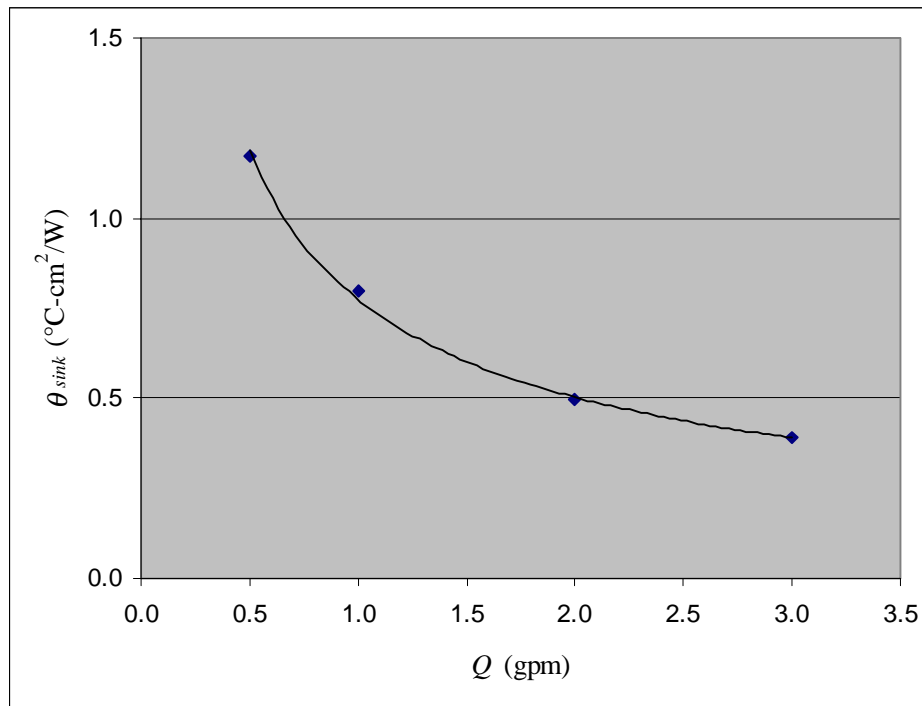


Figure 26. Harris PEBB 1 heat sink average thermal impedance vs. coolant flow rate.

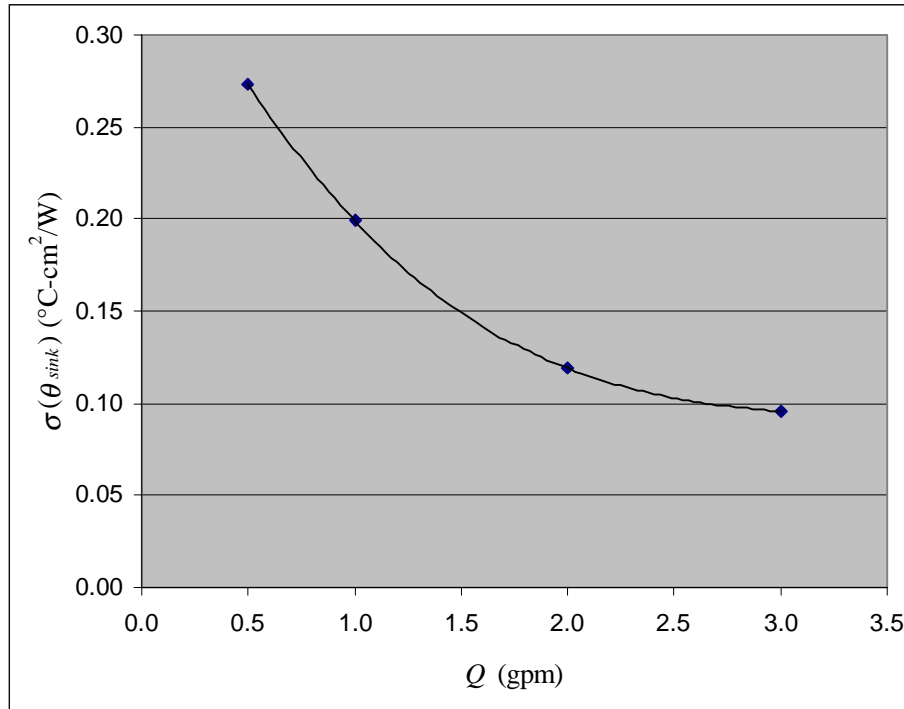


Figure 27. Harris PEBB 1 heat sink thermal impedance standard deviation vs. flow rate.

External System Requirements

Figure 28 is the plot of pressure drop versus flow rate for the Harris PEBB 1 baffled heat sink. This plot illustrates one of the main complaints that were leveled against this heat sink during PEBB 1 testing: the large pressure drops associated with it. With a pressure drop of over 20 psi at 3.0 gpm, the use of this heat sink requires a fairly powerful pump. However, it is felt that the majority of the pressure drop measured across this heat sink, like the baseline, is due to the hose fittings. Support for this conjecture can be found in a comparison between Figure 28 and Figure 22. At 1.5 gpm, the Harris PEBB 1 baffled heat sink passes the same flow rate of water through the fittings as does the baseline at 3.0 gpm, having two ports as opposed to four. The pressure drops for these two cases are 5.0 psi for the Harris PEBB 1 and 4.3 psi for the baseline, a difference of only about 15%. Making the reasonable assumption that the baseline pressure drop is due primarily to the fittings, this would indicate that the same is true for the PEBB 1 heat sink, although to a lesser extent.

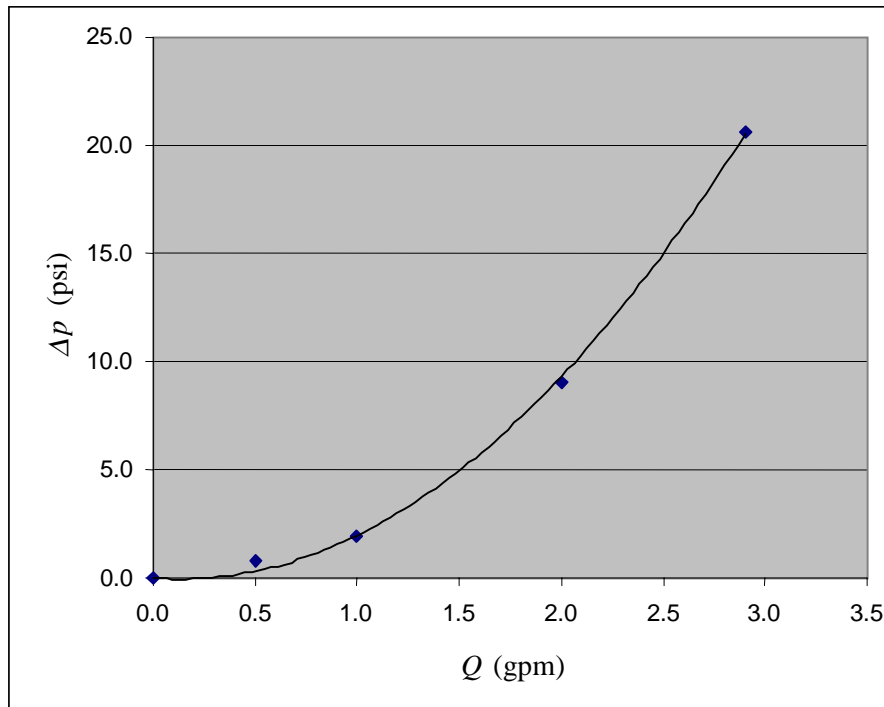


Figure 28. Pressure drop vs. flow rate for Harris PEBB 1 heat sink.

Modified Harris PEBB 1 Baffled

This heat sink was derived from the Harris PEBB 1 design through two minor modifications. The first modification sought to address what was seen as the design's most significant fault: the gap between the top of the partitions and the heat source baseplate. This gap allows a significant portion of the coolant flow to bypass most of the passageways and creates a significant area of poor cooling performance. Addressing this shortcoming was seen as an easy modification and was done by building up the top of the partitions with epoxy until they were flush with the top of the chamber. A less significant change involved the removal of a partition that essentially blocked off part of the chamber and created a stagnant area. The modified heat sink is shown in Figure 29 and the removed partition was in the lower left corner as oriented in the picture. While the raised partitions are difficult to see, the partition removal is easily visible, especially when compared to Figure 23.

Testing of this heat sink was done in an identical manner to that of the unmodified PEBB 1 heat sink. However, due to the more restrictive flow path created by raising the partitions, the pressure drop across the heat sink increased and the maximum flow rate achievable was reduced to 2.9 gpm.



Figure 29. Modified Harris PEBB 1 baffled heat sink.

Thermal Impedance

Figure 30 shows the temperature distribution for the 2.9 gpm, 800 W operating condition and a picture of the heat sink for reference. While these modifications produced significant improvements in the cooling over much of the heat sink, the lower left corner was still not receiving sufficient flow. Because of the high gradients in the temperature distribution in this area, the maximum power level of the test was limited to 800 W in order to avoid cracking the alumina baseplate. An additional modification that probably would further improve the uniformity of the cooling of this heat sink would be to remove the epoxy from the top of the partition between this stagnant area and the return port.

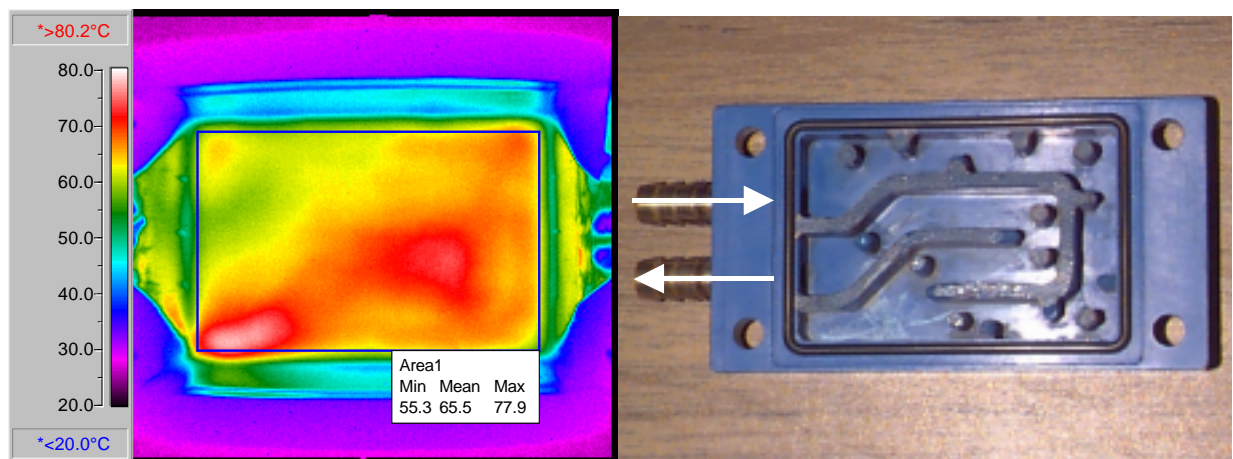


Figure 30. Modified Harris PEBB 1 heat sink temperature distribution at 2.9 gpm flow rate and 800 W dissipation.

The average thermal impedance versus heat flux density for the four flow rates tested are plotted in Figure 31. Once again, the pattern of declining curves with increasing heat flux density is present. The values of the average thermal impedance show a reduction of approximately 25% as compared to the unmodified PEBB 1 results. This is a significant improvement for a minor revision and indicates that the initial design was marginal. It is not hard to imagine a heat sink of similar concept that could achieve results another 25% better than these with a significantly lower pressure drop. The channeled heat sink was an attempt at that ideal; however, it was fabricated before testing was completed on these two versions of the PEBB 1 and therefore did not incorporate all of the lessons learned. As will be seen in the test results contained in this report, that design showed improvements in some areas and was poorer in others.

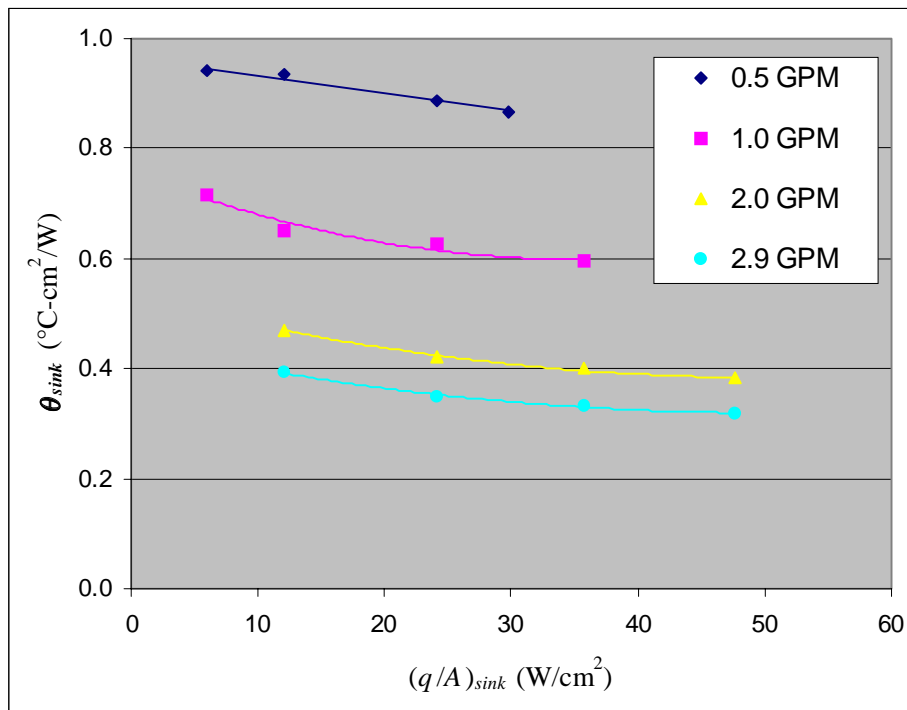


Figure 31. Modified Harris PEBB 1 heat sink average thermal impedance vs. heat flux density.

Figure 32 and Figure 33 are plots of the average thermal impedance and the thermal impedance standard deviation versus cooling water flow rate for the highest heat fluxes reached at each flow rate. The shape of these curves is very similar to those for the other heat sinks. While the average thermal impedance improved by about 25% with the modifications, the standard deviation improved by up to 33% at the lower flow rates and at least 25% at the higher flow rates. It is felt that further significant improvement in the standard deviation would also be achieved by improving the flow to the lower left corner.

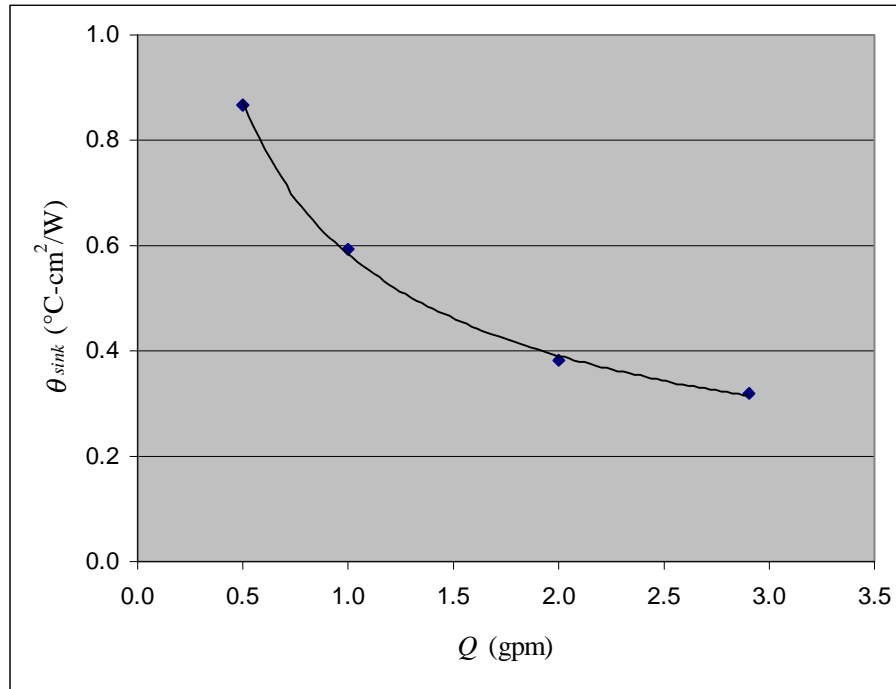


Figure 32. Modified Harris PEBB 1 heat sink average thermal impedance vs. coolant flow rate.

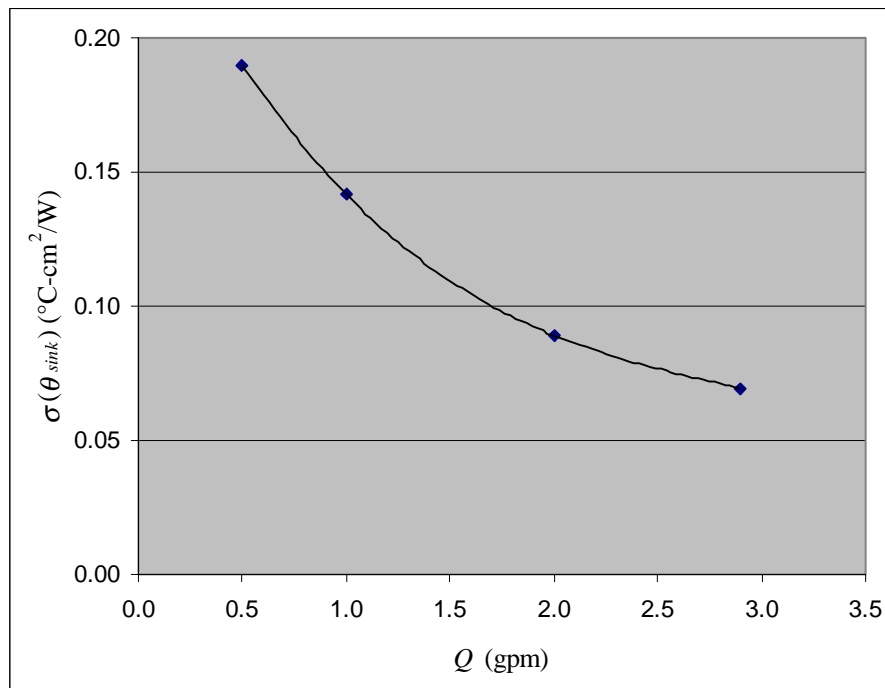


Figure 33. Modified Harris PEBB 1 heat sink thermal impedance standard deviation vs. flow rate.

External System Requirements

The plot of pressure drop versus flow rate for this heat sink is presented in Figure 34. Compared to the original PEBB 1 heat sink, this represents an increase in the pressure drop of about 25%. Once again, most of this occurs at the inlet and outlet ports, however, all of the increase must be due to the modification of the baffles. If it is assumed that the baseline heat sink pressure drop is due entirely to the fittings, then the 15% difference between it and the PEBB 1 mentioned previously is due to the unmodified baffles, leaving 85% for the ports. Based upon this assumption, it can be deduced that just under 70% ($0.85/1.25 = 68\%$) of the pressure drop measured for the modified PEBB 1 heat sink is due to the inlet and outlet ports.

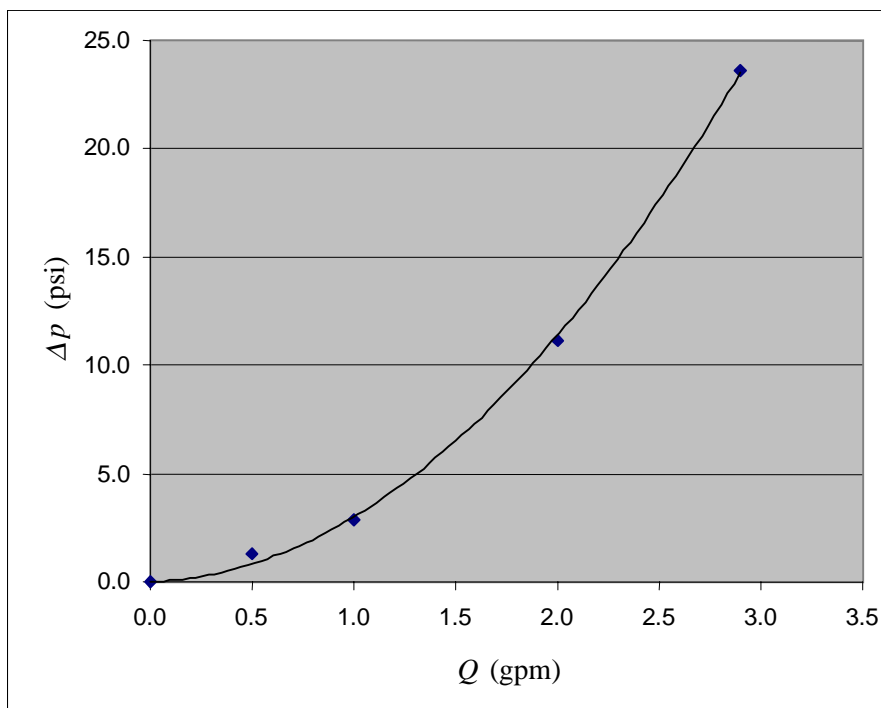


Figure 34. Pressure drop vs. flow rate for modified Harris PEBB 1 heat sink.

Channeled

Shown in Figure 35, the channeled heat sink was designed prior to the start of testing with the intention of addressing two of the shortcomings of the PEBB 1 heat sink that were suspected of causing poor performance in testing by NSWCC. First, it was designed to have the partitions extend all the way to the bottom of the heat source to prevent any significant part of the flow from bypassing parts of the channel. Second, the inlet and outlet ports were enlarged to an inside diameter of a full 1/4" from the 3/16" that the PEBB 1 heat sink used. This increased the cross sectional area of the ports by over 75% and decreased the pressure drop significantly, as will be

seen. The inlet and outlet ports were positioned on the bottom as opposed to the side like the PEBB 1 heat sinks. This was done in order to allow the ports to be positioned at the ends of the four pass channel, which would be more difficult with side mounted ports due to the corner located mounting holes. The cross sectional dimensions of the channels of this heat sink are very close to those of the modified PEBB 1 with the only difference being an approximately 7% increase in the width due to thinner partitions. When the presence of the pins in the PEBB design channels are accounted for as well, the average flow velocity for this design is expected to be somewhat lower than the PEBB heat sinks.

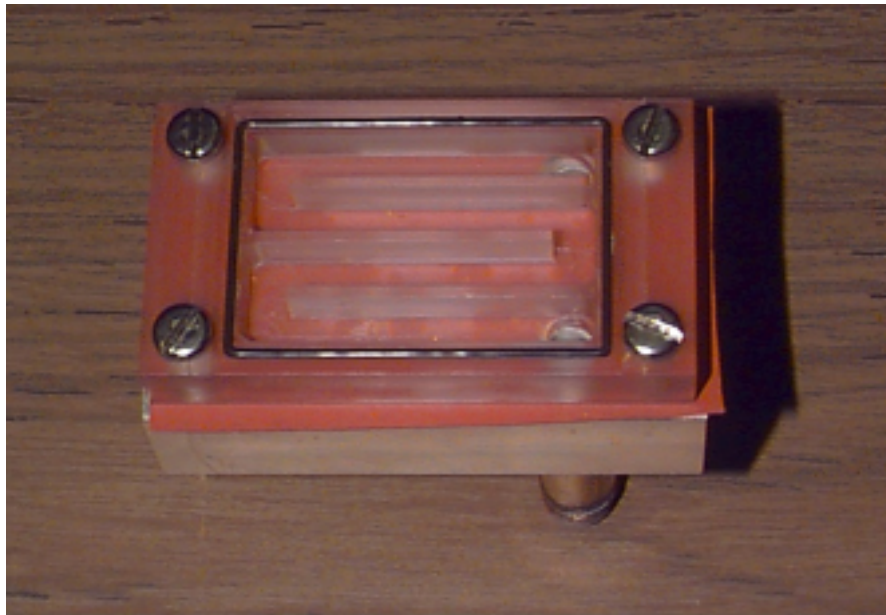


Figure 35. Channeled heat sink.

Testing of this heat sink closely paralleled that of the other heat sinks tested. The primary difference was that 1/2" rubber hose was used to connect the heat sink to the cooling water rather than 1/4" Tygon® tubing. The improvement in the pressure drop across this heat sink allowed a flow rate of 3.5 gpm to be reached during testing.

Thermal Impedance

Figure 36 shows the temperature distribution for the 2.0 gpm, 600 W operating condition and a picture of the heat sink for reference. This operating condition does not represent the highest heat dissipation achieved or the highest flow rate. It is presented here because it is one of the better cases for seeing what is happening in this heat sink while operating. Upon entering the heat sink, the cooling water impinges on the baseplate and provides very good cooling. As the flow progresses down the first straight section, the boundary layer grows and cooling degrades.

Through the first reversal in direction, the boundary layer is reduced in thickness, probably due to some vorticity introduced by the corner. The boundary layer increases in thickness in the second straight section until the next corner, at which point it is reduced again. This pattern repeats for each segment as the flow zigzags through the heat sink with temperatures generally a little higher at the end of each straight segment until the flow reaches the outlet port. This behavior suggests that the use of pins to enhance mixing, as in the Harris PEBB 1 heat sink, probably would be beneficial here.

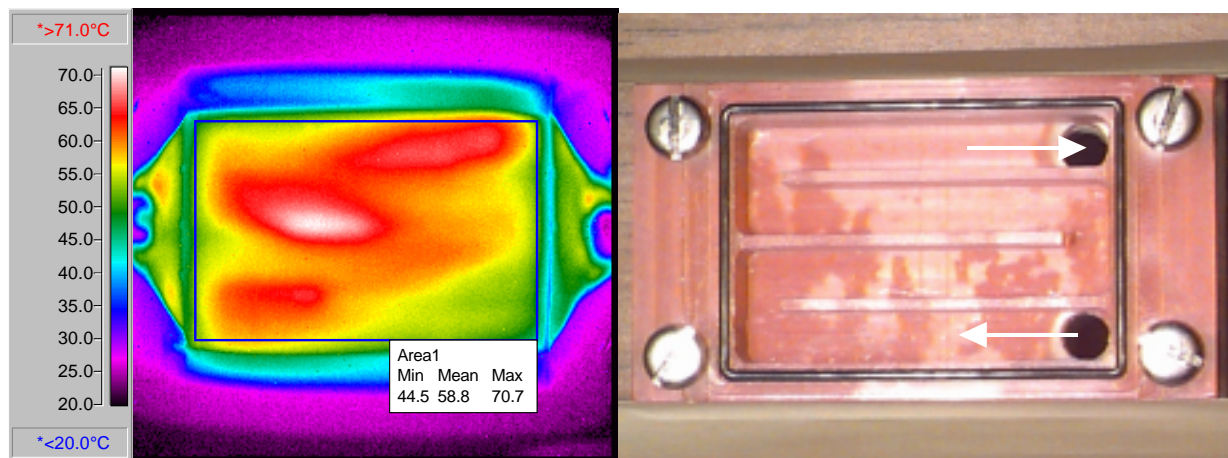


Figure 36. Channeled heat sink temperature distribution at 2.0 gpm flow rate and 600 W dissipation.

The plots of the average thermal impedance versus heat flux density for the five flow rates tested are presented in Figure 37. The first thing that is noticed when examining these curves, compared to all of the other such plots presented thus far, is that the trend of declining curves does not appear for the lower flow rates. In fact, the curves for 0.5, 1.0, and 2.0 gpm actually increase rather than decrease with increasing heat flux density. As will be seen in the thermal impedance standard deviation plot, this heat sink has a very poor uniformity of cooling at these lower flow rates. In addition, the two thermal images captured for the 0.5 gpm, 400 W operating condition had a large variation in average temperature indicating unsteady behavior. These factors make arriving at a conclusion regarding the cause of the increasing curves more difficult. Further study is in order if the true cause is desired. However, since the data was more consistent at the higher flow rates, which is likely where such a heat sink would typically operate, it is not felt that further testing is important at this time.

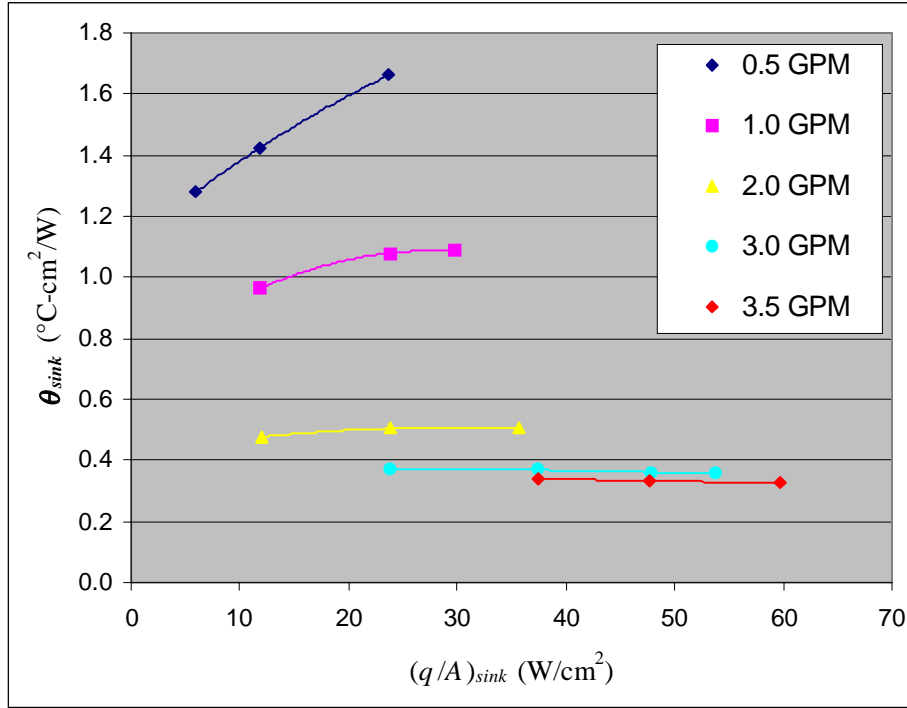


Figure 37. Channeled heat sink average thermal impedance vs. heat flux density.

The average thermal impedance and the thermal impedance standard deviation versus cooling water flow rate are shown in Figure 38 and Figure 39. While this heat sink has both a high average thermal impedance and poor uniformity at low flow rates, as it approaches 3.5 gpm it is comparable to the modified PEBB 1 heat sink operating at its highest flow rate. The difference in performance at lower flow rates is most likely due to the lower average flow velocity, mentioned previously, being insufficient for turbulence. While the average thermal impedance curve has a very similar shape to the same curve for the other heat sinks tested, the standard deviation has a much more dramatic drop versus flow rate than the others do. Having a value of $0.53\text{ }^{\circ}\text{C}\cdot\text{cm}^2/\text{W}$ at 0.5 gpm, the standard deviation also starts off much higher than for any of the other heat sinks tested. It is felt that this heat sink could be significantly improved by making the channels shallower to increase flow velocity for a given flow rate and also by adding features such as pins to increase mixing and promote turbulence. While both of these changes would increase the pressure drop across the heat sink at a given flow rate, good performance would be reached at a lower flow rate in return.

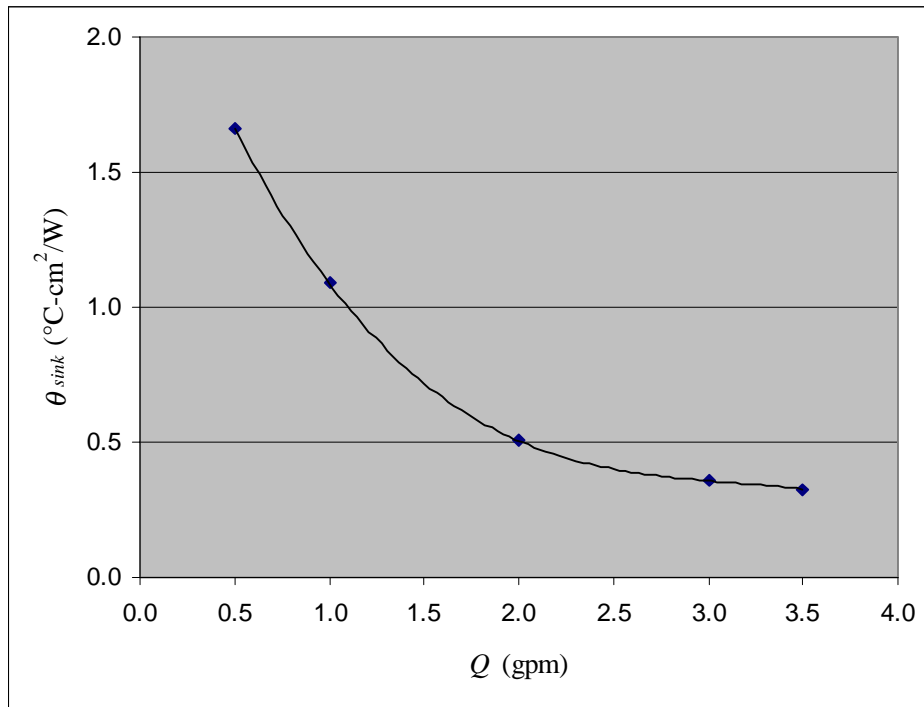


Figure 38. Channeled heat sink average thermal impedance vs. coolant flow rate.

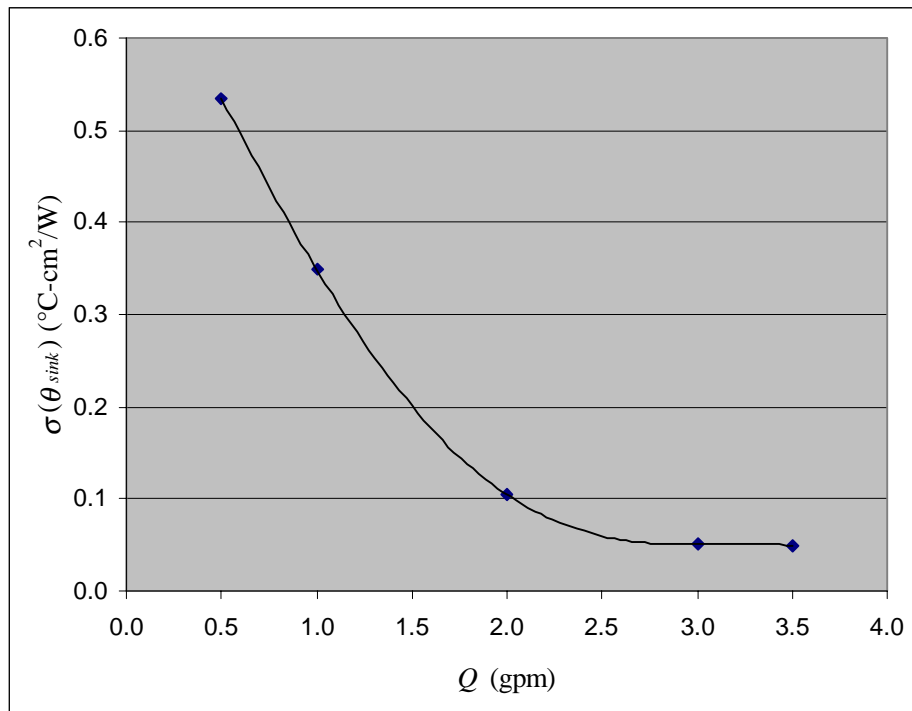


Figure 39. Channeled heat sink thermal impedance standard deviation vs. flow rate.

External System Requirements

The plot of the pressure drop versus flow rate for this heat sink is presented in Figure 40. Compared to the modified PEBB 1 heat sink, this represents a pressure drop reduction of approximately 50% for a given flow rate. However, at any given flow rate, the modified PEBB 1 heat sink has a lower average thermal impedance. A more useful comparison between heat sinks would account for cost of achieving a given level of cooling for a heat sink. Plots of cooling versus pumping power will be presented in the next section comparing the heat sinks tested.

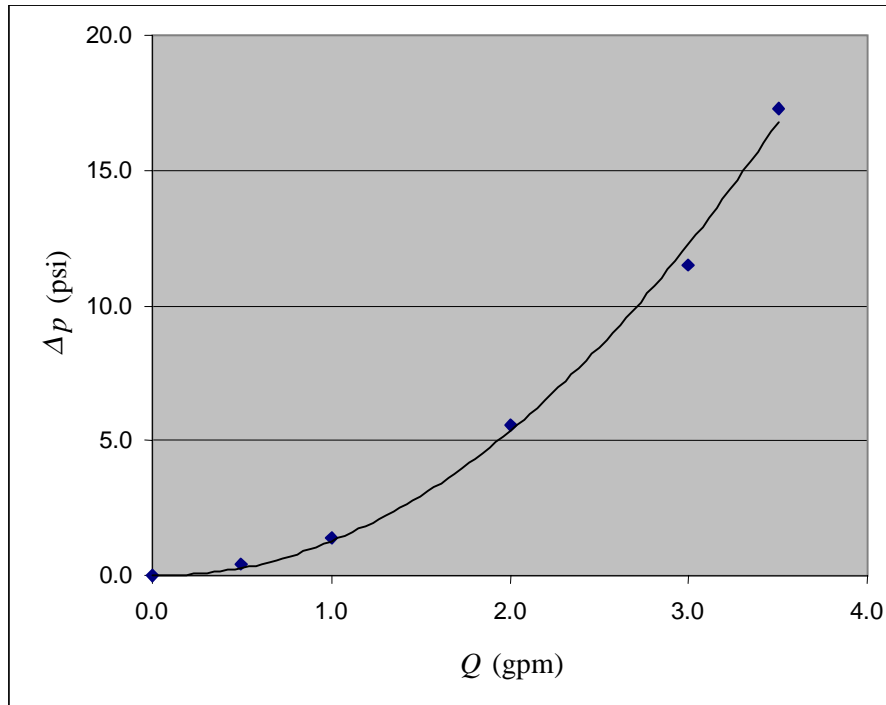


Figure 40. Pressure drop vs. flow rate for channeled heat sink.

Heat Sink Comparison

The plots in Figure 41 through Figure 43 compare the four heat sinks tested in thermal impedance performance versus cooling water flow rate. Figure 41 plots the average thermal impedance versus flow rate and Figure 42 plots the thermal impedance standard deviation versus flow rate. Figure 43 is a plot of the average thermal impedance plus one standard deviation versus flow rate, i.e. the sum of the values plotted in Figure 41 and Figure 42.

In terms of the average thermal impedance plotted in Figure 41, the baseline open chambered heat sink performed poorest across the entire range of flow rates tested and the modified PEBB 1 heat sink performed the best over the test range. The channeled heat sink started off close to the worst at 0.5 gpm and improved to the point that it was very close to the

best at higher flow rates. The poor performance of the open chambered heat sink was expected because it had the largest cross sectional area and thus the lowest average velocity across the plate and it also had no features to enhance mixing. The channeled heat sink's improvement with increasing flow rate to the point of being comparable to the modified PEBB 1 was a little surprising because of its lack of designed-in features to improve mixing. These two being close in performance at higher flow rates is probably due as much to the hot spots in the modified PEBB 1's distribution limiting it as it is to the merits of the channeled design.

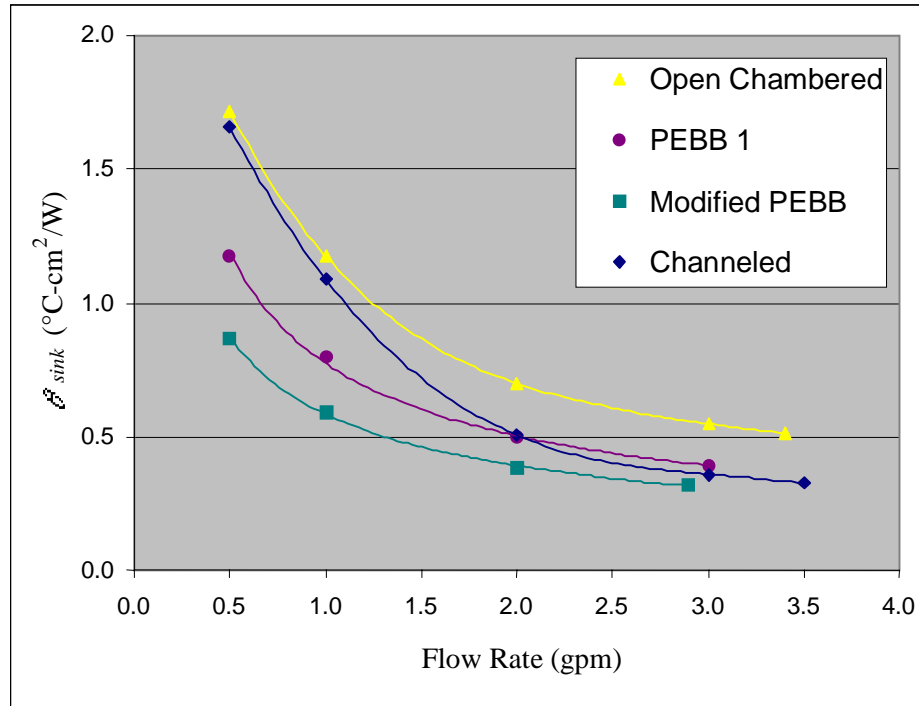


Figure 41. Average thermal impedance vs. flow rate comparison.

The plot of thermal impedance standard deviation versus flow rate, shown in Figure 42, reveals a similar pattern to the average thermal impedance for the channeled heat sink relative to the others, only to a greater extent. At 0.5 gpm it is by far the poorest performer yet it ends up significantly better than the other heat sinks at the peak flow rates. The open chambered and PEBB 1 heat sinks were essentially the same over the entire flow range and the modified PEBB 1 heat sink was consistently about 30% better than those two. The fact that the modified PEBB 1 heat sink had a higher standard deviation than the channeled design at high flow rates shows that hot spots probably limited its average thermal impedance in that range.

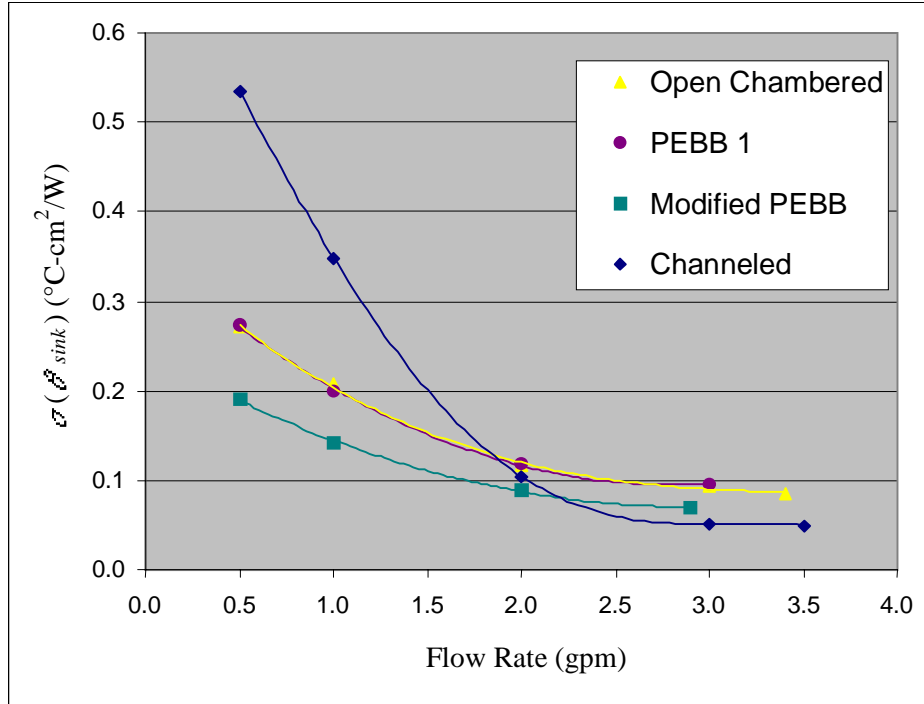


Figure 42. Thermal impedance standard deviation vs. flow rate comparison.

The purpose of the graph in Figure 43, which plots the average thermal impedance plus one standard deviation versus flow rate, is to compare the heat sinks based upon the less effectively cooled areas. For a normal or Gauss distribution of samples, the familiar bell curve, the range from the average minus one standard deviation to the average plus one standard deviation contains 68% of the samples. If the assumption is made that the samples here, i.e. the value of the thermal impedance at each pixel from the infrared image, form a normal distribution, then 84% of the resistor would have a thermal impedance less than the average plus one standard deviation. Therefore, by comparing heat sinks based upon the average plus one standard deviation, a more useful conclusion that accounts for uniformity can be drawn. That is, the majority of the heat sink area can be expected to have thermal impedance values lower than the value plotted in Figure 43. Clearly, at lower flow rates, the modified PEBB 1 heat sink is superior while at higher flow rates, the channeled and the modified PEBB 1 are comparable. The poor uniformity of the channeled heat sink at low flow rates, and its consequent high standard deviation, pushed its curve above that of the baseline open chamber at flow rates up to a little over 1 gpm.

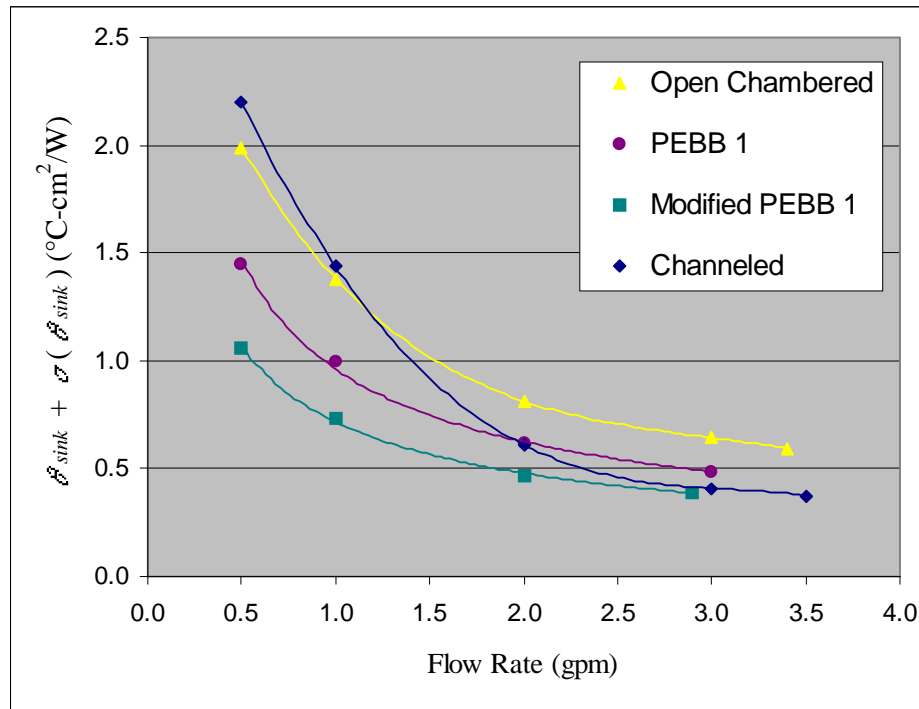


Figure 43. Average thermal impedance plus one standard deviation vs. flow rate comparison.

A plot comparing the pressure drop versus flow rate for the four heat sinks is shown in Figure 44. From this plot, it can be seen that there is a general inverse trend between the thermal impedance of the heat sinks and the pressure drop of the cooling water through them. That is, a heat sink providing lower thermal impedance tends to have a cost in the form of larger pressure drop. This is because good heat transfer from a surface to a fluid comes from having a thin boundary layer with a high thermal gradient within the boundary layer. Good mixing and a turbulent boundary layer produce these characteristics and both of these tend to increase the resistance to flow.

Neither the PEBB 1 nor the modified PEBB 1 were able to exceed 3 gpm due to the limitations of the pump. The open chambered heat sink, while having a curve below the channeled heat sink, was tested to only 3.4 gpm compared to 3.5 gpm for the channeled. This was due to the fixture pressure drop being higher for the open chambered design, which used more fittings and smaller diameter tubing.

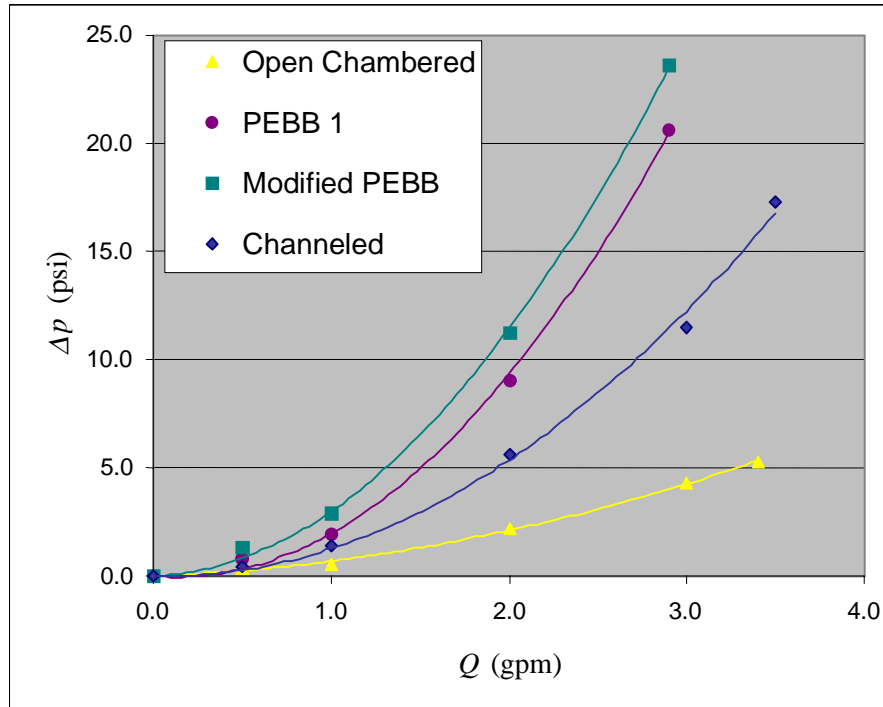


Figure 44. Pressure drop vs. flow rate comparison.

As a means of comparing heat sinks in terms of efficiency, the average thermal impedance plus one standard deviation versus fluid or pumping power dissipated was plotted in Figure 45 and on a log scale in Figure 46. Stating which heat sink is better in these plots depends upon the important design criteria. If a value of the thermal impedance is sought at the lowest pumping power cost, then the left-most curve for that thermal impedance would be best. If the lowest thermal impedance for an available pumping power is sought, then the lowest curve for that pumping power would be best. Of course, none of these heat sinks were optimized to provide the best cooling performance for a given flow rate or pumping power, so these are stated here as guidelines for use in applying such curves from a more thorough study.

Comparing the heat sinks tested thus far, for a desired thermal impedance down to about $0.5\text{ }^{\circ}\text{C}\cdot\text{cm}^2/\text{W}$ or for pumping powers available of 10 W or less, the modified PEBB 1 heat sink would be the best choice. For lower thermal impedance requirements or for greater available pumping power, the channeled design would be chosen. Neither the PEBB 1 nor the open chambered design would be the best choice in either range.

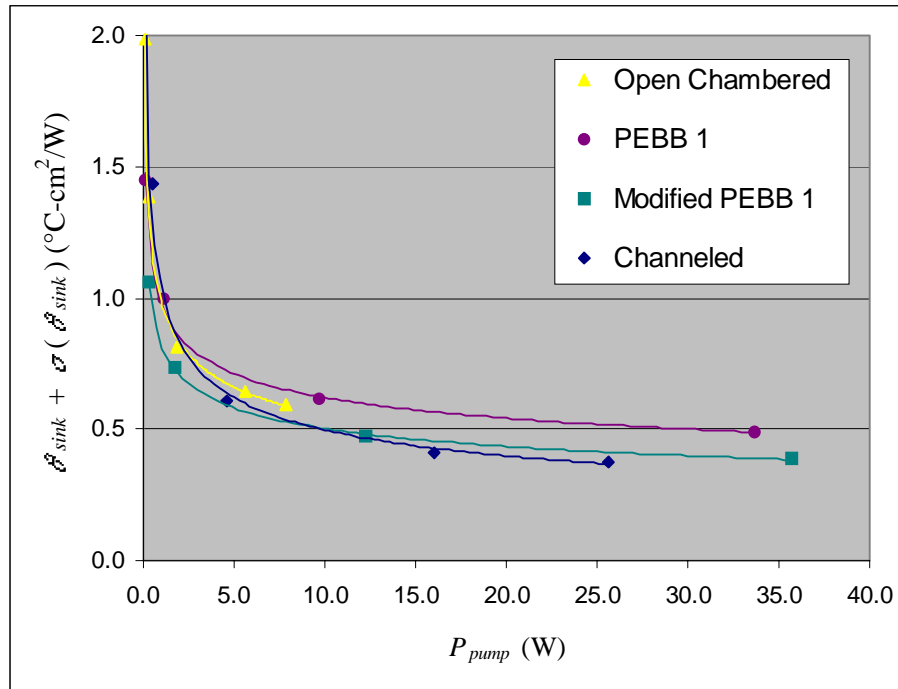


Figure 45. Comparison of average thermal impedance plus one standard deviation vs. pumping power.

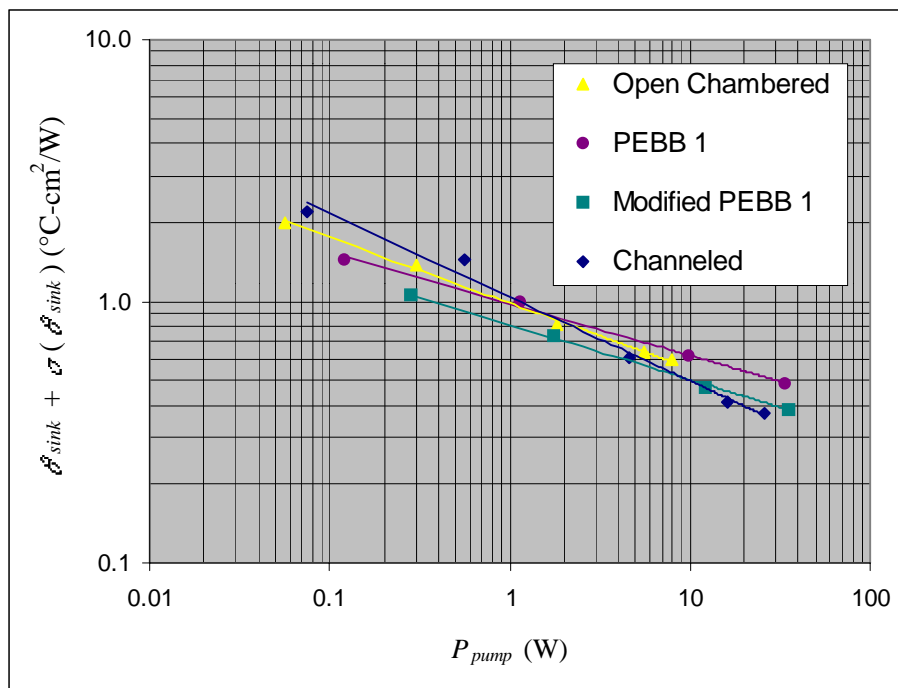


Figure 46. Comparison of average thermal impedance plus one standard deviation vs. pumping power (log scale).

CONCLUSIONS AND FUTURE WORK

Based upon the test results obtained for the open chambered heat sink, it can be concluded that this was not as good a baseline heat sink as was hoped. The combination of two inlet and outlet ports and the use of flexible tubing for the cooling water introduced nonuniform and very unsteady flow to the chamber. Simply moving the supply tubing a few millimeters had a profound effect on the observed TFR temperature distribution. A better baseline would produce a steady and uniform flow across the width of the chamber. A fluid flow manifold was developed for use in testing the copper sponge heat sinks that should do a very good job of producing such a flow. This manifold will be tested to determine if it should be used as the baseline in place of the open chambered heat sink tested here.

The modification to the original PEBB 1 heat sink of raising the partitions so that they almost contact the bottom of the heat source produced a significant improvement in its performance. It forced more of the cooling water flow to wind through the passages rather than over the partitions. This increased the velocity of the flow next to the areas of the baseplate that were not being cooled effectively prior to the modification. It also had the effect of increasing the pressure drop for this heat sink, however, the gains in cooling more than offset these losses.

The results for the channeled heat sink and the two PEBB 1 heat sinks showed that this type of heat sink can be made to perform much better than has been shown here. The simple modifications made to the PEBB 1 heat sink produced significant gains; however, the original layout of the fluid flow path limited the potential of this design. The channeled heat sink showed how a better layout of the passages and improvements to the inlet and outlet ports can produce a more efficient version of this concept, without concentrated hot spots. The visual feedback provided by the thermal images from the testing of the channeled heat sink showed the potential for further improvements by increasing the mixing in the straight sections of the passage. Reducing the depth of the passages to increase the flow velocity for a given volumetric flow rate should also be considered. This would lower overall system cost by reducing the size of the pipes and hoses used to supply water to the heat sink. However, this type of change should not be made to the point that the average temperature of the water increases substantially ($> 10\text{ }^{\circ}\text{C}$) while passing through the heat sink.

The use of a distributed heating source and an infrared thermal imaging camera provides much more thorough information regarding the performance of a heat sink than discrete heat sources and temperature probes. The thermal images from the PEBB 1 and channeled heat sink testing and the information they provided on the distribution of cooling made deficiencies obvious and aided in developing possible ways of improving uniformity and overall

performance. For heat sinks such as the Coriolis curved surface cooling concept, which is inherently non-uniform in the cooling they provide, information from testing using this apparatus will be useful for mapping the thermal impedance to assist designers in locating dies. However, because the TFR is a large distributed heat source and silicon dies are much smaller, the thermal impedance measured here is not directly translatable to a device thermal resistance. While some work has been done in the area of determining thermal resistance from these measurements, more is needed in this area.

During testing, a few changes to the test apparatus that might improve results were postulated. The first would replace the thick film resistor with a thin film resistor. Thin film resistors are deposited on the substrate using a plating or sputtering process as opposed to the printing of a paste and subsequent firing for thick film resistors. This tends to produce a resistive layer that is much more uniform in thickness. The drawback to this type of resistor is that it is a metallic resistor material and therefore tends to be much more reflective. This problem could be alleviated through the use of a coating on top of the resistor made of a material with properties better suited to infrared thermography. This change will be considered for use in future testing if additional resistors need to be made.

Another change that will be tried in future testing is the use of a portable chamber around the resistor and heat sink to provide controlled background radiation conditions. This chamber would have sufficient ventilation to prevent the temperature inside from elevating while having an interior surface with uniform emissivity. Therefore, once calibration is done for the background radiation, more consistent and accurate results should be obtained as compared to a room background which may have people or other sources of infrared radiation moving around.

The primary issue concerning the results obtained thus far that needs to be addressed in future work is that of the declining curves of thermal impedance versus heat flux density. As mentioned previously, measurement error will be addressed through better control of the background radiation. The other speculated cause, the change in properties of the cooling water with film temperature, will also be examined further. This will likely be accomplished through comparison to analytical results using both simple empirical boundary layer heat transfer relations as well as finite element analyses. Further results and correlation from analytical modeling that is in progress will also be presented including the effects of scaling.

Further testing which needs to be completed include evaluation of the Coriolis curved surface cooling heat sink and the Harris/SPCO copper sponge heat sink. Testing of both of these heat sinks was delayed due to difficulties in attaching the TFR heat sources to them. Initial attempts to solder both of these to the metalized back side of the alumina substrate met with

failure. Part of the problem was the result of the metalization leaching off of the alumina; however, after that problem was corrected by using solder with a 2% silver content, further difficulties were encountered with achieving a uniform bond. Anticipated solutions to these problems are to have a company experienced in large area soldering do the sponge attachment and to use a thermal adhesive to attach the curved surface heat sink.

Another issue that has been examined is the use of aluminum silicon carbide (Al/SiC) composite material as part of the power module packaging. This material can be made to have a coefficient of thermal expansion (CTE) very close to that of silicon as well as alumina or aluminum nitride, thereby minimizing thermal stresses. While this adds an additional layer to the power module's package and therefore increases its thermal resistance, it improves durability as compared to an exposed ceramic baseplate and reliability as compared to a copper baseplate. It can also be molded to form integral pin-fins for improved convection heat transfer from the module. Therefore, the net effect may be only a slight degradation in steady-state thermal dissipation capability and an improvement in transient performance due to increased thermal mass.

REFERENCES

1. Eades, Herbert H., "Thermal Modeling of Hybrid Microelectronics," Masters Thesis, Virginia Tech, July 1990.

APPENDIX A. UNIT CONVERSIONS

<u>Variable</u>	<u>Metric</u>	<u>Multiply by</u>	<u>English</u>	<u>Conversion Description</u>
A	cm ²	0.1550	in ²	surface area
h	W/cm ² -°C	1.761×10 ³	Btu/hr-ft ² -°F	film coefficient
k	W/cm-°C	57.78	Btu/hr-ft-°F	thermal conductivity
L, Δ	cm	0.3937	inch	length
L, t	μm	3.937×10 ⁻⁵	in	length and thickness
q, P	W	3.412	Btu/hr	heat dissipation, power
Q	l/s	15.85	gpm	flow rate
q/A	W/cm ²	3.171×10 ³	Btu/hr-ft ²	heat flux
t	cm	393.7	mil	thickness
T	°C	32+1.8×°C	°F	temperature
Δp, p	Pa	1.450×10 ⁻⁴	psi	pressure
θ	cm ² -°C/W	5.678×10 ⁻⁴	hr-ft ² -°F/Btu	thermal impedance

NOTATION

Acronyms

A&T	Analysis and Technology
HTP	Harris Thin Pack
IGBT	Insulated-Gate Bipolar Transistor
IR	Infrared
MCT	MOS-Controlled Thyristor
NSWCCD	Carderock Division of the Naval Surface Warfare Center
ONR	Office of Naval Research
PEBB $x.x$	Power Electronic Building Block, version number
TFR	thick film resistor

Symbols

Δp_{gauge}	differential pressure gauge reading
ε	emissivity
$\theta(x,y)$	thermal impedance
$\theta_{sink}(x,y)$	thermal impedance of the heat sink
$\theta_{TFR}(x,y)$	thermal impedance of thick film resistor assembly
$\theta_{TOT}(x,y)$	thermal impedance from TFR to water
σ	standard deviation
A	area
Bi	Biot number
F	function
h	film coefficient
I	current
I_{res}	current through resistor
k	thermal conductivity
p_{in}	supply water pressure
p_{out}	return water pressure
P	power
Pr	Prandtl number
q	heat flux
$(q/A)_{heating}$	heat transfer rate per unit area produced by resistive heating of TFR

$(q/A)_{rad+conv}$	heat transfer rate per unit area convected and radiated from TFR surface
$(q/A)_{sink}$	heat transfer rate per unit area into heat sink
Q	flow rate
Re	Reynolds number
t	thickness
$T(x, y)$	temperature distribution at heat sink interface
T_{AL}	average temperature of TFR alumina
T_F, T_{in}	inlet temperature of cooling fluid
T_{out}	outlet temperature of cooling fluid
$T_{TFR}(x, y)$	temperature distribution of thick film resistor
T_{res}	average temperature of TFR
T_1	temperature at the bottom interface of a layer
T_2	temperature at the top interface of a layer
V_{res}	voltage across resistor
V	voltage

Units

cm	centimeter
cm ²	square centimeter
xx°	degrees
°C	degrees Centigrade
x''	inch
psi	pounds per square inch
gpm	gallons per minute
μm	micrometers (10 ⁻⁶ meter)
mil	milli-inch (10 ⁻³ inch)
Ω	ohm
%	percent
W	watts